



저작자표시-비영리-변경금지 2.0 대한민국

이용자는 아래의 조건을 따르는 경우에 한하여 자유롭게

- 이 저작물을 복제, 배포, 전송, 전시, 공연 및 방송할 수 있습니다.

다음과 같은 조건을 따라야 합니다:



저작자표시. 귀하는 원저작자를 표시하여야 합니다.



비영리. 귀하는 이 저작물을 영리 목적으로 이용할 수 없습니다.



변경금지. 귀하는 이 저작물을 개작, 변형 또는 가공할 수 없습니다.

- 귀하는, 이 저작물의 재이용이나 배포의 경우, 이 저작물에 적용된 이용허락조건을 명확하게 나타내어야 합니다.
- 저작권자로부터 별도의 허가를 받으면 이러한 조건들은 적용되지 않습니다.

저작권법에 따른 이용자의 권리는 위의 내용에 의하여 영향을 받지 않습니다.

이것은 [이용허락규약\(Legal Code\)](#)을 이해하기 쉽게 요약한 것입니다.

[Disclaimer](#)

공학석사 학위논문

**Experimental Measurement and Force
Balance Analysis of Sliding Vapor Bubble
Behavior on a Horizontal Tube**

수평관 표면 활주 비등 기포에 대한
실험적 관측 및 힘 평형 분석

2017년 8월

서울대학교 대학원
에너지시스템공학부
김 유 나

Experimental Measurement and Force Balance Analysis of Sliding Vapor Bubble Behavior on a Horizontal Tube

수평관 표면 활주 비등 기포에 대한
실험적 관측 및 힘 평형 분석

지도교수 조 형 규

이 논문을 공학석사 학위논문으로 제출함

2017 년 8 월

서울대학교 대학원

에너지시스템공학부

김 유 나

김유나의 석사 학위论문을 인준함

2017 년 8 월

위 원 장 김 응 수 (인)

부위원장 조 형 규 (인)

위 원 김 석 (인)

Abstract

Experimental Measurement and Force Balance Analysis of Sliding Vapor Bubble Behavior on a Horizontal Tube

Yu-Na Kim

Department of Energy System Engineering

The Graduate School

Seoul National University

Boiling on the outer surface of a horizontal tube occurs in various systems including PAFS, which is the passive residual heat removal system of APR +. In order to predict the boiling heat transfer based on a kinematic model such as the heat partitioning model, it is important to understand the behavior of the vapor bubbles. Particularly, in the case of the lower inclined surface such as the lower half of a horizontal tube, the accuracy of the heat transfer prediction depends on the evaluation of the sliding bubble motion. However, previous studies on bubble behavior mainly focused on the horizontal plate or the vertical channels, and the experimental and analytic studies on the sliding bubble behavior on a horizontal tube were insufficient. Therefore, the purpose of this study is as follows. First, measuring the sliding bubble behavior parameters experimentally, required for the improvement of the heat transfer model. Second, analyzing the sliding bubble behavior using the improved force balance model to establish the foundation of

the predictable model.

In order to observe the sliding bubble behavior on the outer surface of a horizontal tube heater, the experimental facility with a horizontal tube heater was constructed. In addition, the stereoscopic measurement technique using the two synchronized high-speed cameras was established. The experiment was performed using nearly saturated water under atmospheric pressure for various conditions; liquid velocity (11.2 – 27.6 mm/s), wall heat flux (26 – 66 kW/m²), and the location of nucleation site (0 – 180° from the bottom of the heater). A thin film heater with a narrow heating strip proposed in this study generates boiling bubbles in a restricted region on a horizontal heater. Therefore, the quality of the visualization of the sliding bubbles improved significantly. Furthermore, an artificial cavity created on the heating strip could control the location of the nucleation cavity so that it improved the surface condition difference between the polyimide-based heater and the metal heater.

The two synchronized high-speed cameras captured the behavior of the bubbles from two perpendicular measurement angles. The configurations of the bubbles were identified by an image processing method based on shadowgraphy from the two images, and the results of the image processing includes various boiling bubble parameters, such as the departure and lift-off of bubble, bubble volume transient, bubble velocity, bubble frequency, etc. In particular, the volume of the non-spherical bubble was calculated by a three-dimensional reconstruction method, which defines a specific cross-section configuration at each elevation using stereoscopic images. The two verification steps confirmed that the reconstruction method has allowable errors and the monoscopic visualization method has a limitation for deformed bubble measurement.

Based on the experimental observations, the force balance analysis of the sliding bubble on the horizontal tube was performed. The previous force balance model for the sliding bubble on a horizontal plate was improved for sliding bubble on the horizontal tube by introducing additional forces and representing them in cylindrical coordinates. The circumferential force balance analysis estimated the local liquid velocity, not obtained in experiment. The radial force balance analysis estimated the local liquid velocity gradient and predicted the lift-off point of the sliding bubble. As a result, the dominant forces determining bubble behavior confirmed in this study are the surface tension, contact pressure force, buoyancy and added mass force. Meanwhile, the lift force, buoyancy and added mass force are dominant near the lift-off. Finally, the study based on the experimental observation and analysis results figured out the transients of the bubble behavior parameters. It could be the foundation of developing a prediction model of bubble behavior by simplifying and improving on several parameters.

.....

Keywords: Boiling heat transfer, Horizontal tube, Sliding bubble behavior, Stereoscopic observation method, Image processing technique, Force balance analysis

Student Number: 2015-22940

List of Contents

Abstract	i
List of Contents	iv
List of Tables.....	iv
List of Figures.....	iv
Chapter 1. Introduction	1
1.1 Boiling heat transfer on a horizontal tube	2
1.2 Previous studies on bubble behavior	3
1.3 Objectives of this study	6
Chapter 2. Experimental Facility	9
2.1 Test loop	9
2.2 Horizontal tube heater with a narrow heating strip for bubble visualization	11
2.3 Visualization system.....	14
Chapter 3. Establishment of Measurement Method.....	21
3.1 Phase separation technique.....	21
3.1.1 Axial image.....	22
3.1.2 Radial image.....	23
3.2 Measurement of bubble parameters.....	24
3.3 3 dimensional bubble reconstruction technique	27
3.3.1 Bubble reconstruction procedure	27
3.3.2 Verification of reconstruction technique	28
3.3.2.1 Verification for inclined ellipsoids.....	28
3.3.2.2 Verification for asymmetric phantom images	30

3.4 Measurement results	32
Chapter 4. Force Balance Analysis	48
4.1 Force balance model for a sliding bubble on the horizontal tube 48	
4.2 θ -directional force balance analysis	50
4.3 R-directional force balance analysis.....	53
4.4 Analysis result	56
Chapter 5. Closure of Force Balance Model	66
5.1 Empirical correlation for bubble behavior parameters.....	66
5.1.1 Local liquid velocity	66
5.1.2 Bubble deformation coefficient	67
5.1.3 Radius of curvature of the bubble at the heater surface ...	67
5.1.4 Contact angle	68
5.1.5 Velocity gradient correction factor.....	69
5.1.6 Limitation in the closure	69
5.2 Prediction result	70
Chapter 6. Conclusion.....	82
6.1 Summary.....	82
6.2 Recommendation.....	83
Reference	85
국문 초록	89

List of Tables

Table 1.1 Experimental and observation conditions of previous studies regarding sliding bubbles.	7
Table 3.1 Test matrix.....	34

List of Figures

Figure 2.1 Schematic diagram of the bubble visualization test loop (unit: mm).	16
Figure 2.2 Bubble visualization test loop.....	17
Figure 2.3 Axial (left) and radial (right) views of sliding bubbles on a conventional cartridge heater.....	17
Figure 2.4 Film heater with narrow heating width: (a) Stainless steel circuit on the polyimide substrate, (b) CAD image of the film heater.	18
Figure 2.5 Schematic side view of the film heater.....	18
Figure 2.6 Film heater installed in the test section (left) and sliding bubbles on narrow heating region (right).....	19
Figure 2.7 Change of bubble diameter transient by the artificial cavity.	19
Figure 2.8 Schematic diagram of visualization system setup.	20
Figure 2.9 Axial (left) and radial (right) images of sliding bubbles on a film heater, observed using two synchronized cameras.	20
Figure 3.1 Image processing procedures for the phase separation of axial image.....	35
Figure 3.2 Image processing procedures for the phase separation of radial image.....	36
Figure 3.3 Definition of bubble parameters: bubble frequency, contact length, lift-off, velocity.	37
Figure 3.4 Bubble departure identification.....	37

Figure 3.5 Procedure of the cross-section accumulation: (a) line connection between the top and bottom points, (b) cross-section reconstruction.	38
Figure 3.6 Synchronized axial image (left), reconstruction result image (middle) and synchronized radial image (right): (a) 90° nucleation location, (b) 23° nucleation location.	39
Figure 3.7 Reconstruction result of bubbles in various views.	39
Figure 3.8 Inclined oblate ellipsoid based on configuration of observed bubble.	40
Figure 3.9 Examples of ellipsoids by observation angles.	40
Figure 3.10 Verification of reconstruction methods for inclined ellipsoids: ...	41
(a) Errors of monoscopic reconstruction by sphericity and observation angle,	41
(b) Errors of stereoscopic reconstruction by sphericity and observation angle.	41
Figure 3.11 Asymmetric phantom objects (observation angle: 0°, 90°).	42
Figure 3.12 Verification of reconstruction methods for asymmetric phantom images: (a) Errors of monoscopic reconstruction by sphericity and observation angle, (b) Errors of stereoscopic reconstruction by sphericity and observation angle.	43
Figure 3.13 Measured bubble volume transient with various bulk liquid velocity of 135° nucleation location.	44
Figure 3.14 Measured bubble volume transient with various bulk liquid velocity of 45° nucleation location.	44
Figure 3.15 Measured bubble volume transient with various bulk liquid velocity of 23° nucleation location.	45
Figure 3.16 Relation between transients of bubble equivalent diameter and contact line length.	46
Figure 3.17 Measured bubble frequency with various heat flux of 45° nucleation location.	47
Figure 3.18 Measured bubble velocity with various bulk liquid velocity of 23° nucleation location.	47

Figure 4.1 Forces acting on a sliding bubble.....	58
Figure 4.2 Force balance model: (a) in θ -direction, (b) in r-direction.	59
Figure 4.3 Estimated local liquid velocity: (a) 23° nucleation location, (b) 45° nucleation location.	60
Figure 4.4 Velocity gradient correction factor relative to local liquid velocity.	61
Figure 4.5 Liquid velocity gradient at bubble centroid: (a) slow liquid velocity, (b) fast liquid velocity.	61
Figure 4.6 Result of radial force balance analysis: (a) 23° nucleation location, (b) 45° nucleation location.	63
Figure 4.7 Bubble trajectory tracked by the force balance model on overlapped experimental image: (a) 23° nucleation location, (b) 45° nucleation location.	64
Figure 4.8 Prediction result of the improved force balance model: (a) sliding length, (b) lift-off diameter.	65
Figure 5.1 Empirical correlation of local liquid velocity: (a) 23° nucleation location, (b) 45° nucleation location.	72
Figure 5.2 Schematic diagram about calculation of contact angle.	73
Figure 5.3 Coefficient in empirical correlation of bubble volume.	73
Figure 5.4 Bubble trajectory tracked by the force balance model with empirical correlations of 23° nucleation location: (a) 26kW/m ² , 11mm/s, (b) 26kW/m ² , 22mm/s, (c) 26kW/m ² , 28mm/s, (d) 30kW/m ² , 11mm/s, (e) 30kW/m ² , 22mm/s, (f) 30kW/m ² , 28mm/s.	76
Figure 5.5 Bubble trajectory tracked by the force balance model with empirical correlations of 45° nucleation location: (a) 26kW/m ² , 11mm/s, (b) 26kW/m ² , 22mm/s, (c) 26kW/m ² , 28mm/s, (d) 30kW/m ² , 11mm/s, (e) 30kW/m ² , 22mm/s, (f) 30kW/m ² , 28mm/s, (g) 49kW/m ² , 22mm/s.	80
Figure 5.6 Prediction result of the improved force balance model with empirical correlations: (a) sliding length, (b) lift-off diameter.....	81

Chapter 1.

Introduction

Boiling bubble behavior on heating surfaces have been studied intensively in the field of engineering to accumulate knowledge of the boiling heat transfer mechanism and to develop a better model based on the bubble dynamics. There has been significant progress in the study of two-phase flow and boiling heat transfer with advances in the experimental techniques and modeling capability with CFD (Computational Fluid Dynamics). The advanced experimental instruments, such as high-speed cameras, PIVs (Particle Image Velocimetry), infrared cameras, etc., enable the production of high-resolution local information of boiling bubble behavior, such as bubble configuration, velocity, and bubble-wall interaction (Okawa et al., 2005; Duan et al., 2013; Yoo et al., 2014; Jung et al., 2016; Chu et al., 2016). In conjunction with these improvements in experimental techniques, various attempts have been made to predict the boiling heat transfer using a CFD code in a mechanistic approach by considering the bubble behavior on the heating surface, such as departure, lift-off, and sliding (Kurul et al., 1990; Sateesh et al., 2005; Luke et al., 2000; Sugrue et al., 2014). However, these experimental and modeling efforts have been principally focused on horizontal plates or vertical channels, and not many studies have been conducted for the outer surface of a horizontal heater in spite of its practical importance in heat exchanger design and analysis.

1.1 Boiling heat transfer on a horizontal tube

In particular, an advanced pressurized light water nuclear reactor APR+ (Advanced Power Reactor +) incorporates a passive auxiliary feedwater system, which supplies feedwater to a steam generator using gravitational force and natural circulation without any electrical power for active driving mechanisms (Kang et al., 2012). This system includes a horizontal tube bundle submerged in a large water pool. Boiling occurs outside of these heat exchanger tubes by the heat transferred from the tube, where high pressure steam condensation occurs. For this reason, understanding of the boiling heat transfer on a horizontal tube surface became an important issue to evaluate the performance of the passive system of the advanced nuclear reactor (Jeon et al., 2015). This background motivated the present study to visualize a boiling bubble and its sliding motion on a horizontal heater.

A simulation of boiling heat transfer using the two-fluid model (or time-averaged model) of a CFD code, requires the boiling heat transfer model to evaluate the phase change rate under given flow and wall conditions. The widely accepted boiling heat transfer model for CFD codes is the heat partitioning model (or RPI model) proposed by Kurul et al. (1990), which decomposes the boiling heat transfer into three mechanisms; evaporation, transient heat conduction, and single-phase convection. Since its development, a number of modifications were made for this model to improve its accuracy and applicability. For example, Basu et al. (2005) proposed a modified heat partitioning model with the addition of a heat transfer term influenced by a sliding bubble. However, most of these models were developed and validated for plates or vertical channels and few models are

available for a horizontal tube outer wall boiling bubble. Sateesh et al. (2005) proposed a modified heat partitioning model applicable to not only vertical plates, but also a horizontal tube. The model considers the sliding bubble motion and the resulting thermal boundary layer disruption, and it was validated against two horizontal tube boiling experiments performed by Barthau and Hahne (2000) and Luke and Gorenflo (2000).

1.2 Previous studies on bubble behavior

The key submodels of these heat partitioning models are related to bubble behavior, including the bubble growth, departure, sliding, and lift-off, since they affect the boiling heat transfer significantly. The understanding of this boiling bubble behavior, therefore, is a crucial factor in predicting the boiling heat transfer rate accurately. Since the bubble parameters are determined by competition among forces exerted on the bubble, predicting these parameters using the force balance equation has been endeavored. Klausner et al. (1993) proposed a widely accepted bubble force balance model under the saturated forced convection condition on a horizontal plate. The forces acting on an asymmetric single bubble were analyzed with bubble configuration and flow conditions and the bubble departure and lift-off diameters can be predicted as a result. This model is applicable to both pool boiling and flow boiling conditions, and was validated based on data from tests performed with refrigerant R113 as the working fluid. Yeoh and Tu (2004) extended Klausner's force balance model to a vertical heating surface and applied the modified model to a CFD simulation of subcooled boiling at low pressure in a

vertical annulus channel. Yun et al. (2012) improved the force balance model to extend its applicability to subcooled boiling at high pressure in a vertical pipe. Recently, Surge et al. (2014) established and extended the force balance model to predict the bubble departure and lift-off at various surface orientations. However, further investigation and validation are required in order to extend its applicability to a horizontal heat exchanger tube because most of the validation works have been conducted with plate geometries or vertical channels.

Table 1.1 summarizes experimental efforts to visualize the boiling bubble behavior on a heating surface and its condensation after lift-off. Thorncroft and Klausner (1998) examined the boiling phenomena on vertical heating surfaces in the upward and downward forced convection conditions, as well as pool boiling conditions. The bubble growth, departure, lift-off, waiting time, etc. were measured using a high-speed camera. The bubble growth and its deformation during sliding were observed furthermore. Situ et al. (2005, 2008) also measured various bubble behavior parameters from the side in parallel with the heater and proposed correlations for the parameters with respect to flow conditions.

Recently, there are some previous studies which applied a stereoscopic method, which observes a single object in different directions, in order to consider the deformation of sliding or rising bubbles (Zaruba et al., 2007; Murai et al., 2001; Maurus et al., 2004; Fujiwara et al., 2004; Bian et al., 2013). These works pointed out the limitation of the monoscopic observation method when it was applied to a nonspherical bubble. Okawa et al. (2005) observed a sliding bubble inside a vertical cylindrical tube using two synchronized cameras installed in the tangential and normal directions to the heating surface. The shape of a bubble is considered to be an ellipsoid which has three different axis lengths obtained from

two images. Yoo et al. (2014) investigated the bubble behavior on a vertical plate under forced convection conditions. According to this observation at the moment of bubble departure, the bubble shape in the image obtained from the view parallel to the heating surface approximates an ellipse, but that from the perpendicular view shows a circle. Thus, the bubble was regarded as a prolate or oblate ellipsoid for volume evaluation. Kim et al. (2011) measured the condensation rate in the subcooled boiling condition after bubble departure in the bulk liquid region. The stereoscopic method, followed by the three-dimensional image reconstruction method, was proposed for an accurate measurement of the condensation rate. Imaginary phantoms were used to quantify the uncertainties of the stereoscopic observation method depending on the deformation extent. Since the deformation of a bubble is significant in boiling on a horizontal tube according to open literature (Cornwell et al., 1982; Kang, 2005), Kim et al.'s reconstruction method for a deformed bubble was adopted in the present experiment.

There are experimental visualization results for the sliding bubble motion on a downward facing inclined heating surface. Qiu and Dhir (2002) performed a pool boiling experiment with an inclined plate with a refrigerant as the working fluid. Bouncing motion of the bubble during sliding was observed and the mechanism was expressed with the lift force and recoil force. Sugrue et al. (2014) conducted a series of subcooled boiling experiments in forced convection and measured the bubble departure diameter under various flow, subcooling, heat flux, and pressure conditions. These experimental observations of bubbles on inclined plates have given important insight to understand bubble motion including sliding on a horizontal heater. However, the inclination of a horizontal tube surface varies continuously along the circumference and therefore, the findings of the inclined

channel tests may not be applied directly to horizontal tube boiling. In this context, there are not sufficient experimental data on horizontal tube boiling, and are even less on the detailed bubble motions. This lack of experimental data on horizontal tube boiling and the bubble behavior became the motivation for an experiment which can provide detail information on bubble behaviors for the force balance model validation and improvement.

1.3 Objectives of this study

In order to improve the heat transfer model for a horizontal tube heat exchanger, the implementation of experimental database should be prioritized. Furthermore, prediction models for sliding bubble behavior are required to estimate some important parameters included in the heat transfer model such as heat partitioning model. Therefore, this study was conducted with sequential objectives as follows.

- Establishment of measurement and visualization techniques for sliding bubble
- Measurement of various bubble parameters
- Force balance analysis to understand sliding bubble behavior
- Closure of force balance model

Table 1.1

Experimental and observation conditions of previous studies regarding sliding bubbles.

	Klausner et al. (1993)	Thorncroft and Klausner (1998)	Qiu and Dhir (2002)	Basu et al. (2005)
Geometry	Square channel	Square channel	Square channel	Square channel
Flow direction	Horizontal	Vertical (up flow, down flow, pool)	Inclined direction (5-75°)	Vertical
Working fluid	R113	FC-87	PF-5060	Water
Heater surface	Copper	Nichrome	Kapton foil (polyimide) polished silicon wafer	Copper
Pressure	Atmospheric pressure	Atmospheric pressure	Atmospheric pressure	103–320 kPa
Fluid subcooling	Saturation	1–5°C	0.7–5°C	2–52.5°C
Flow velocity	112–287 kg/m ² s (75.3–194.1 mm/s)	190–666 kg/m ² s (111–385 mm/s)	Pool	124–926 kg/m ² s
Heat flux or wall superheat	11.0–26.0 kW/m ²	1.32–14.6 kW/m ²	0.58–6°C	25–900 kW/m ²
Measured parameters	Departure diameter	Growth rate, departure and lift-off diameter, waiting time	Bubble shape, trajectory, growth rate, velocity	Bubble frequency, waiting time, departure diameter, nucleation site density, etc.
Measurement view	Parallel	Parallel	Parallel and perpendicular	Parallel: bubble volume, frequency. Perpendicular: nucleation site density
Bubble departure or lift-off diameter	Departure diameter: 0.1– 0.7 mm	Departure diameter: 0.1–0.3 mm		Departure diameter: 0.05–0.15 mm

	Situ et al. (2005,2008)	Okawa et al. (2005)	Kim et al. (2011)	Yoo et al. (2014)	Sugrue et al. (2014)
Geometry	Annulus	Cylindrical tube	Square channel	Square channel	Square channel
Flow direction	Vertical	Vertical	Vertical	Vertical	Inclined direction (0,30,45,60,90,180°)
Working fluid	Water	Water	Water	Water	Water
Heater surface	Cartridge heater	Sapphire glass tube coated ITO	Copper coated Teflon	Glass coated ITO	Stainless steel (316L)
Pressure	Atmospheric pressure	121–127 kPa	105 kPa	Atmospheric pressure	101, 202, 505 kPa
Fluid subcooling	1.5–20°C	2.2–10°C	14.9–24.7°C	14°C	10, 20°C
Flow velocity	473–930 kg/m ² s	94–1435 kg/m ² s	85 kg/m ² s	216–424 kg/m ² s	250, 300, 350, 400 kg/m ² s
Heat flux or wall superheat	60.7–206 kW/m ²	54–338 kW/m ²	60.06–122.81 kW/m ²	10.6–24.3 kW/m ²	50, 100 kW/m ²
Measured parameters	Lift-off diameter, departure frequency	Bubble shape, lift-off diameter, velocity	Bubble shape, condensation rate	Bubble shape, departure frequency	Departure diameter
Measurement view	Parallel	Tangential and normal	Parallel and perpendicular	Parallel and perpendicular	Parallel
Bubble departure or lift-off diameter	Lift-off diameter: 0.2–0.5 mm	Lift-off diameter: 0.5–4 mm		Departure diameter: 0.25–0.5 mm	Departure diameter: 0.2–1 mm

Chapter 2.

Experimental Facility

2.1 Test loop

The schematics of bubble visualization test loop are presented in Figs. 2.1 and 2.2. It was designed to perform a saturated flow boiling experiment under atmospheric pressure conditions with water as the working fluid. The test loop consists of the water storage tank, water supply pump, preheater, test section, heat exchanger, and optical devices. Subcooled water in the storage tank is driven by a centrifugal water pump, and the flow rate is controlled by the motor frequency control using an inverter. The water flows into the preheater region, where cartridge heaters are installed to heat the fluid up to the saturation temperature. This heater was also used for the degassing procedure. Downstream of the preheater, a flow straightener and perforated plates were installed to flatten the velocity profile at the test section inlet. The test section is a 0.11×0.11 m square duct of 0.5 m length, as shown in Fig. 2.1. It incorporates a horizontal rod heater at the mid-elevation, on which the boiling occurs. The heater rod is made of a polycarbonate rod, with a film heater attached to it. The details of the film heater and the visualization strategy are discussed in the following sections. The dimensions of the square duct and the rod diameter were determined by using the

design information of the passive auxiliary feedwater system and the PASCAL test facility (Kang et al., 2012). The exit of the test section is connected with a plate type heat exchanger to cool the water and condense the vapor. Cooling water is supplied to the secondary side of heat exchanger by a chiller. The cooled water is stored in the storage tank. At the top of the storage tank, a reflux condenser is attached and it returns the condensate to the tank during the degassing procedure and operation, thereby preventing evaporation loss of the water after a long operation.

The measurement instruments for the global parameters and their uncertainties are summarized below. The liquid mass flow rate is measured by Coriolis flow meter RHM-17498 (Rheonik) and it has a 0~4.17 kg/s measurement range with under $\pm 0.3\%$ measurement error. The test section inlet pressure is measured by Rosemount 2051CG with $\pm 0.01\%$ span error, and the differential pressure between the inlet and outlet of the test section is measured by Rosemount 2051CD with $\pm 0.02\%$ span error. T-type thermocouples supplied by Omega are used for the liquid temperature measurement with $\pm 1^\circ\text{C}$ measurement error. The thermocouples are installed at the water storage tank, pump inlet and outlet, preheater chamber, test-section inlet and outlet and downstream of the heat exchanger. The local bubble parameters are measured by two high-speed cameras using the digital image processing technique, and the details are discussed in chapter 3.

2.2 Horizontal tube heater with a narrow heating strip for bubble visualization

For the measurement of the bubble parameters, such as bubble departure diameter, bubble lift-off diameter, and sliding distance on a horizontal heating surface, the visualization from the axial direction of the horizontal rod would be advantageous compared to that from the radial direction because the bubble-wall interaction can be more clearly identified with the former. However, it is difficult to visualize the bubble motion from the axial direction if a conventional cartridge heater is used for the boiling experiment, where multiple nucleation sites are activated and overlapping of the bubble images cannot be avoided. This overlapped bubble image hinders observation of the bubbles near the heating wall, as well as an accurate analysis of the bubble motions, as shown in Fig. 2.3.

Furthermore, a deformed bubble is expected to appear on an inclined downward heating surface owing to the forces exerted by the buoyancy and drag forces. If the deformation from the sphere is considerable, monoscopic visualization using one single camera, either from the axial or radial direction of the horizontal rod, cannot provide accurate information on the deformed bubble volume and evaporation rate. As shown in Fig. 2.3, significantly deformed bubbles were observed in the preliminary test using a conventional cartridge heater. These limitations in visualization using a conventional heater for the accurate measurement of deformed bubbles motivated the design of a particular heater adequate for sliding bubble motion visualization.

In the present study, a film heater with a narrow heating region was utilized. It was intended to generate bubbles on a narrow strip in a circumferential

direction on the horizontal rod by restricting the heating region. Figs. 2.4-(a) and (b) show a two-dimensional drawing of the film heater attached to the horizontal rod and its three-dimensional view, respectively. The film heater was fabricated on a polyimide substrate in conjunction with an etching process, and a thin stainless steel circuit on the polyimide substrate was used as the heater. The circuit includes a localized area-reducing part for an electrical current, as illustrated in Fig. 2.4-(a), where the resistive heating is activated. The narrow strip was designed with width in range of 0.5-3.0 mm. The preliminary experiment using the heaters with various width confirmed that the heater with width greater than 1 mm does not distort the phenomena. Thus, all subsequent experiments were conducted using the 3 mm wide heater.

The circuit was insulated using a polyimide cover lay film and accordingly, the boiling occurs on the outer surface of this film. It was attached to the 50 mm polycarbonate rod using an adhesive and its schematic side view of the film heater is presented in Fig. 2.5. The heater rod was installed in the test section in the horizontal direction and aligned to locate the heating part at the center of the test section width. The electric current was supplied by a DC power supply connected to the electrodes in Fig. 2.4-(a).

Fig. 2.6 shows the installed film heater in the test section and the observed bubbles on the devised film heater. As intended, bubbles were generated on the narrow heating region and overlap of the bubbles, which obstructs the observation of sliding bubbles, was prevented. Application of this heater and a stereoscopic visualization method were successful, which facilitated enhanced bubble volume measurement and evaporation rate evaluation.

At the beginning of this experiment, the heater was used without artificial

control of surface condition such as artificial cavity. Instead, a particular spot is activated as a nucleation site prior to its adjacent region. Once a bubble is generated, the bubble moves upward sliding on the heated surface, and it disturbs the superheated liquid layer. Due to this agitation effect, other nucleation sites are rarely activated downstream of the nucleation site. As a result of this characteristic, it is possible to visualize the bubbles generated at one particular nucleation site, even if the artificial cavity is not fabricated on the heater. Moreover, the location of the nucleation site at a specific angle is enabled by rotation of the heater.

The characteristics of the boiling phenomena are greatly influenced by surface conditions. The roughness of polyimide surfaces in the present experiment was 11 nm similar with the values in Fiorenza et al. (2013), 12~35 nm, while metallic surfaces are rougher, with values in the order of 100–1000 nm. The contact angle of the polyimide surface is about 76.7° within the range of 73.8~76.9° reported in other literatures, such as Cho et al. (2005) and Gotoh et al. (2003), and the value after boiling changes to 50.3° in the present experiment. These values of the surface roughness and contact angle can cause phenomenological differences in boiling and bubble behaviors depending on the surface characteristics of the reference surface. Thus, they can impose constraints on the produced experimental data when applying them directly to a practical situation.

Thus, in order to overcome the limitation of the roughness difference and to control the location of a nucleation site systematically, an artificial cavity was made by SUS pin with a diameter of about 50 μ m diameter on the narrow heating region. As a result, it was confirmed that the bubbles generated from the artificial cavity are much smaller than that of spontaneous cavity and have similar lift-off

diameter to the bubbles generated on metal surface, as presented in Fig. 2.7 (Ryu et al., 2014). However, since it is a temporary solution to improve the difference in surface condition, further experiment will be conducted using the silicon rubber heater covered by a copper film.

2.3 Visualization system

In the present experiment, deformation of the bubble occurs while it slides on the curved heating surface. In order to measure the volume of the deformed bubble, a stereoscopic visualization technique was established. The visualization systems for the bubble motion measurement comprise two synchronized high-speed cameras, which were aligned to capture the same bubble motion from two different measurement angles (frame rate: 1000 Hz); the axial and radial directions of the horizontal rod. The cameras are IDT Motionpro Y4 and Phantom V711-16G-M with fast options for the former and the latter, respectively. Three xenon-lamps were used as the light source; two lamps were located on the opposite side of each camera for shadowgraphy and the other supported the discernment of the bubble departure and lift-off by lighting a specific spot on the tube. A schematic diagram of visualization system setup is shown in Fig. 2.8.

Fig. 2.9 shows a pair of example images recorded by the two synchronized cameras. As shown in the figure, bubble phases are observed darker than other side due to the refraction of backlight in the bubbler. Shadowgraphy is image

processing technique which separates bubble phase from the image of two-phase flow using the brightness intensity.

In order to obtain the geometrical information of bubbles using these two images, two image processing steps are required; the first step is the separation of bubble phases from the background image, and the second is the three-dimensional bubble reconstruction. Details of each process are described in the following sections.

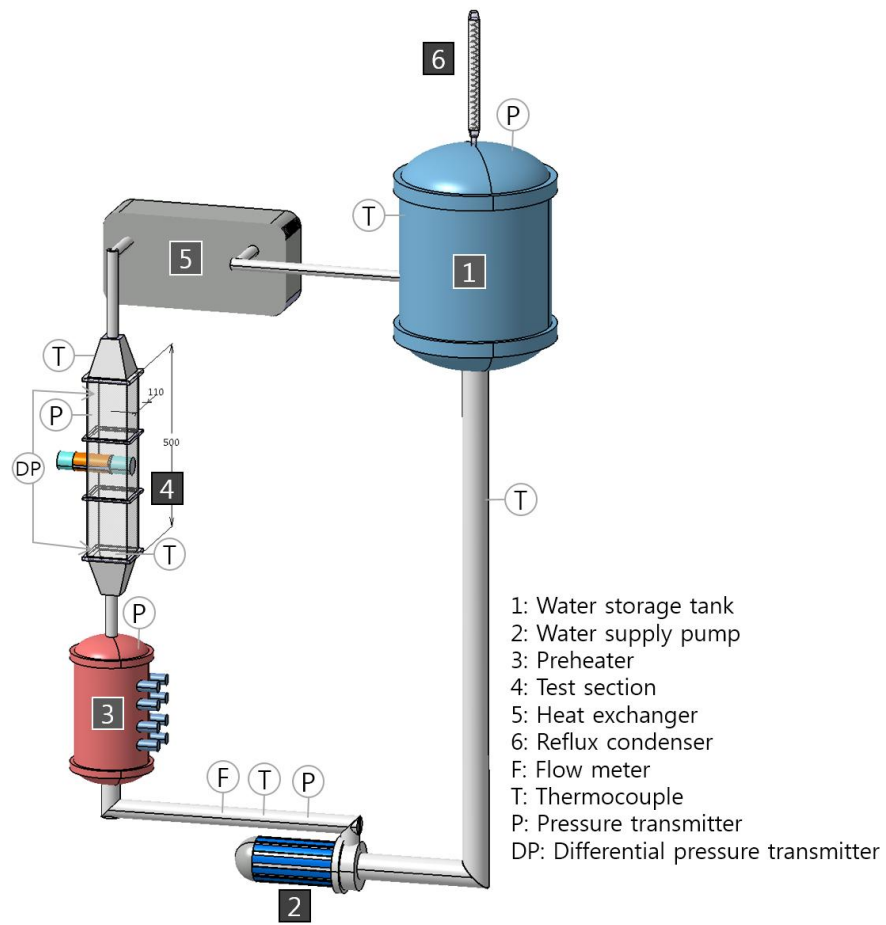


Figure 2.1 Schematic diagram of the bubble visualization test loop (unit: mm).

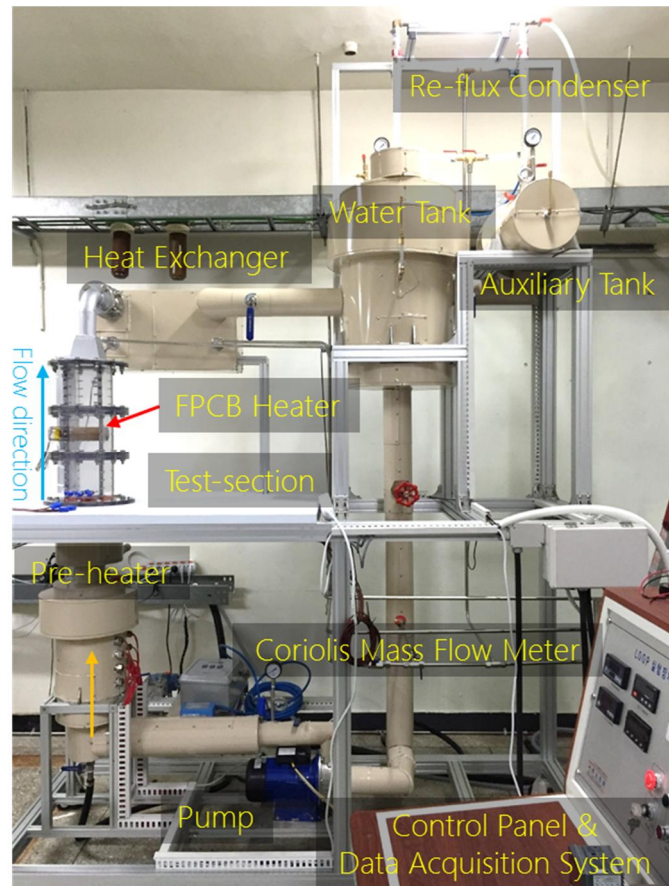


Figure 2.2 Bubble visualization test loop.

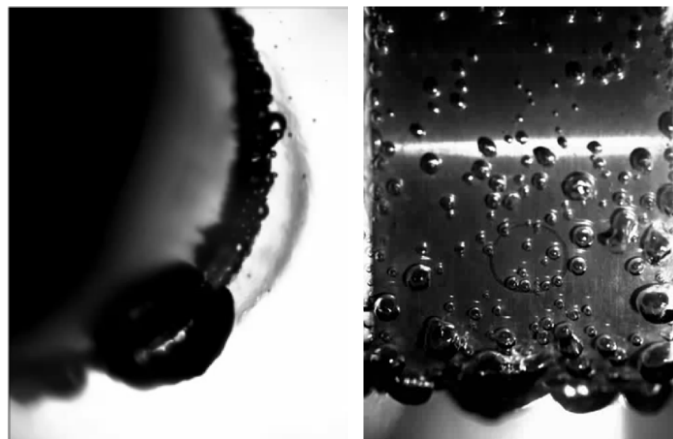


Figure 2.3 Axial (left) and radial (right) views of sliding bubbles on a conventional cartridge heater.

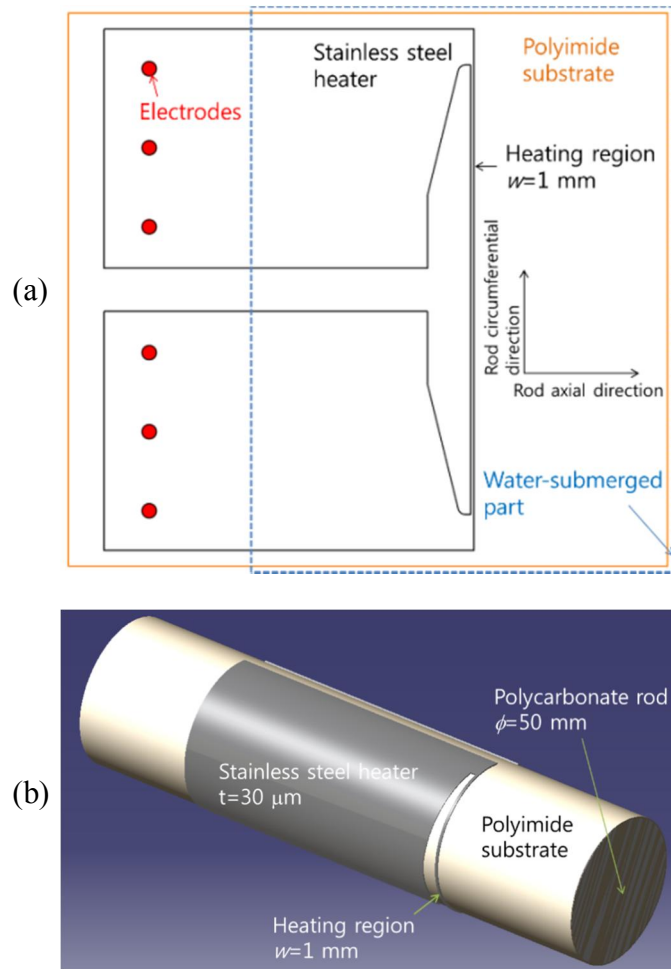


Figure 2.4 Film heater with narrow heating width: (a) Stainless steel circuit on the polyimide substrate, (b) CAD image of the film heater.

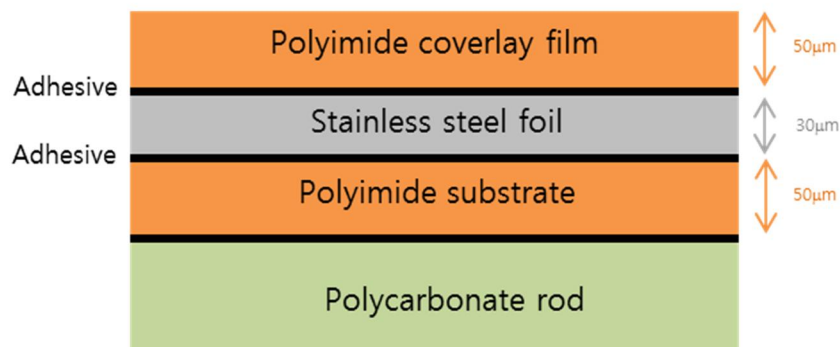


Figure 2.5 Schematic side view of the film heater.

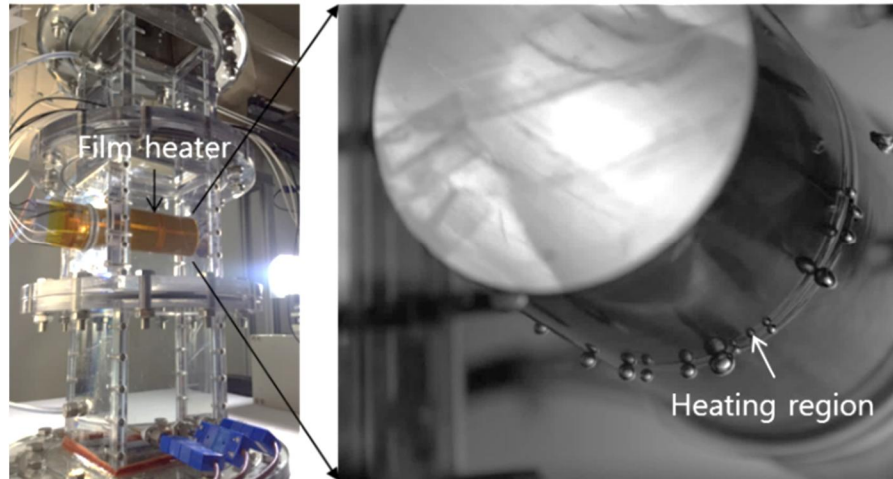


Figure 2.6 Film heater installed in the test section (left) and sliding bubbles on narrow heating region (right).

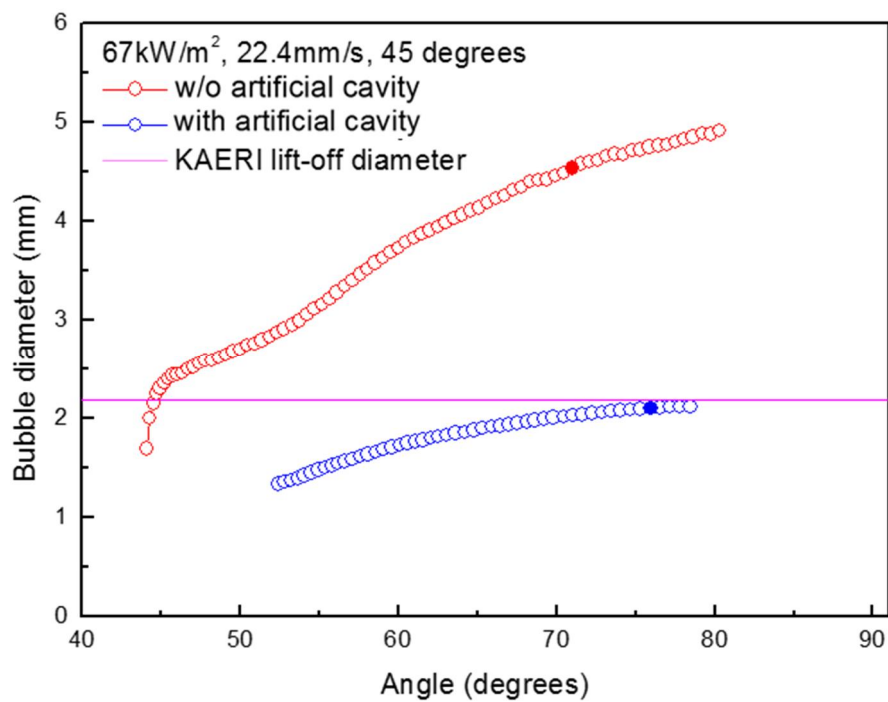


Figure 2.7 Change of bubble diameter transient by the artificial cavity.

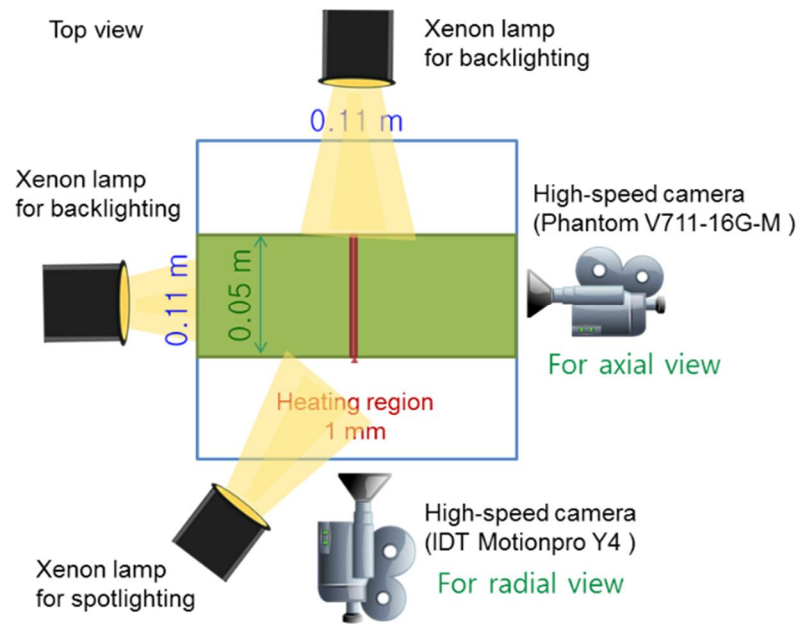


Figure 2.8 Schematic diagram of visualization system setup.

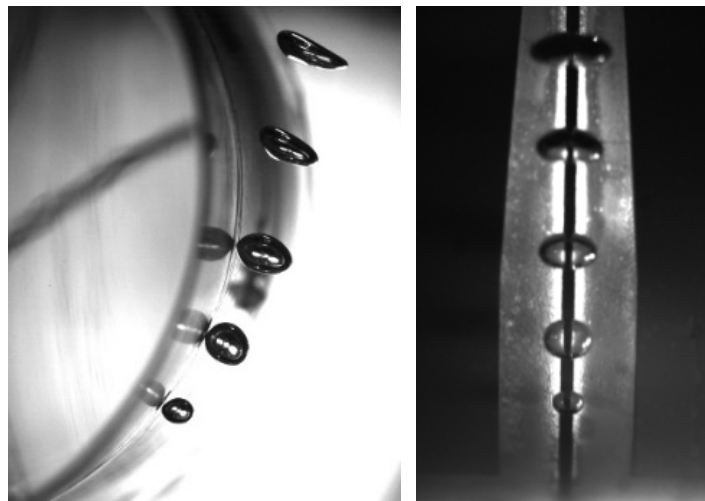


Figure 2.9 Axial (left) and radial (right) images of sliding bubbles on a film heater, observed using two synchronized cameras.

Chapter 3.

Establishment of Measurement Method

3.1 Phase separation technique

The visualization setup of this study produces bubble phases darker than the background due to refraction of the backlight hence, the shadowgraphy method was adopted. It uses this brightness intensity difference between two phases to separate the bubbles in the image from the background. The image was processed using the MATLAB image toolbox (The MathWorks, 2014). The procedures for phase separation are slightly different depending on the direction of the observation. The axial directional images can provide crucial information on the bubble sliding motion and wall-bubble interaction. Therefore, the image processing was mainly established with the axial images, and the other was used to obtain information required for the bubble configuration determination.

3.1.1 Axial image

The image processing procedure for phase separation of axial image is summarized below, and exemplified in Fig. 3.1.

- (1) Subtract the background from the original image and complement the light intensity
- (2) Remove the shadow of bubble and heat waves near the heater surface: Designating the area near the heater surface using a masking image, set the high intensity criteria only to remove the shadow or heat waves.
- (3) Add the area of reflected light: Add the area, which is observed bright due to reflection on the bubble interface and the heater surface.
- (4) Binarize the intensity image and fill holes surrounded by white pixels: The intensity threshold is decided as a proper threshold value given by Otsu's method.
- (5) Smooth the detected edge using eroding, dilating, convex hull processes, etc.
- (6) Verification using the overlapped image: The edges of the identified bubbles were overlapped with the original image for verification of the algorithm

3.1.2 Radial image

Although the basic process is similar to that of the axial image, there is a difference in detail due to different illumination. The process is summarized below, and illustrated in Fig. 3.2.

- (1) Subtract the background from the original image and complement the light intensity
- (2) Remove the shadow of bubble on the opposite side of the light source (the left side of the heating strip)
- (3) Add the area of reflected light on a the right side of the heating strip
- (4) Binarize the intensity image and fill holes surrounded by white pixels
- (5) Restore the bubble shape on the heating strip: Bubble phases could not be observed on the heating strip, since the strip obstructs backlight from reaching the bubbles. For the restoration, two component of bubble phase separated by the strip were connected.
- (6) Remove the incomplete configuration and process the contour: When the nucleation site is located below, initial bubbles are difficult to be observed due to difference of the focus distance. The removed configuration was replaced by a circle.
- (7) Verification using the overlapped image

Finally, the separated bubble phases are resized by the height of the axial configurations, since the radial bubble shapes may be observed in different sizes due to perspective.

3.2 Measurement of bubble parameters

The image reconstruction provides detailed information of the bubble configuration. By numerical integrations of the cross-sectional area and circumference at each pixel elevation, the bubble volume and interface area can be calculated, respectively. The evaporation rate of the bubble can be evaluated with the volume change over a certain duration multiplied by the latent heat. Bubble departure and lift-off are two of the most important parameters of the heat partitioning model, and the force balance model is required to predict these in a mechanistic way. In the present study, these parameters were measured by the image processing.

- **Bubble frequency and bubble generation**

In the present experiment, a single nucleation site of the heater was activated. If a new bubble is detected in the frequency counting region near the nucleation site, shown in Fig. 3.3, the moment is considered to be bubble incipience and the bubble frequency is calculated by counting the number of detected bubbles. At the

same time, the newly generated bubble is given a unique number that identifies the bubble among the other sliding bubbles. Thus, the experimental data can be organized with the unique number of bubbles.

- Bubble velocity

The bubble velocity can be obtained with the displacement of the bubble centroid in unit time. Its coordinate change was calculated as shown in Fig. 3.3 with the green line, which was created by merging two consecutive images, and the velocity was calculated by dividing it by the time passed between the two consecutive images.

- Contact diameter

In the axial image, a line on which a bubble makes contact with the heater surface is defined as the contact line, as indicated in Fig. 3.3 with blue lines. The contact line includes both the dry-out region and the microlayer region as the present visualization method cannot identify them separately.

- Bubble departure and lift-off

The length change of a contact line provides information to discern the moment of bubble departure and the lift-off. In the bubble growth period, the contact line is prolonged and the end points of the line move in the opposite

direction; the lower one moves downward and the upper one upward (Fig. 3.4-(a) → Fig. 3.4-(b)). Shortly prior to departure, the lower one moves upward, whereas the upper end point is almost stationary (Fig. 3.4-(b) → Fig. 3.4-(c)). At the moment of bubble departure, both the lower and upper end points moved in the same upward direction, and this criterion was defined as the bubble departure moment. This definition was adopted considering particular characteristics of the surface geometry and the bubble motions of the present experiment. The departure diameter may be identified when the location of bubble centroid moves in the upward direction. However, in the present experiment, it moves upward even though the bubble is apparently attached on the nucleation site and it is because the bubble is shifted upward due to the buoyancy force and drag force. Thus, early departure was identified with this criterion. The upward location change of the contact line center can be used as the bubble departure identification criterion. But, in the present experiment, the bubble grows asymmetrically and the contact line does not elongate symmetrically. For this reason, the criterion was not adequate for the bubble departure identification and the present criterion was selected. Meanwhile, the identification of the bubble lift-off is recognized if the contact length reduces from a positive value to zero.

3.3 3 dimensional bubble reconstruction technique

3.3.1 Bubble reconstruction procedure

The detected edges of bubbles were used for the reconstruction of bubble interfaces in three-dimensions to evaluate their volumes, growth rate, equivalent diameters at the moment of the bubble departure and lift-off, and so on. This bubble reconstruction method, modified from the method proposed by Kim et al. (2011), was adopted in the present study, and Fig. 3.5 illustrates the procedure.

First, a straight line connecting the topmost and bottommost points of the bubble was created as shown in Fig 3.5-(a) indicated with the green line (reference line). In the present study, it was assumed that this line is shared by the two images from different angles. This assumption is reasonable if there is no concave part and the concave part is hardly observed in the present experiment while a bubble is attached on the heating surface thanks to the surface tension. After that, another assumption is applied that the boundary of the bubble in the radial view (red line) is located on the red line in the axial view. In the same manner, the blue line is dealt with. The x- and y- coordinates of points laying on these lines at each elevation z were determined from the radial and axial view images, respectively. These points were set as the reference points at each elevation. Then, four lines connecting the boundary edge of the bubble and the reference point at an elevation were created, Line-1~Line-4 in Fig. 3.5-(b). These four lines established the x- and y- intercepts of an enclosure representing the bubble cross-section configuration. Finally, the other assumption is applied that a cross-section of the bubble at an elevation is reconstructed by combining four

pieces of different ovals as indicated in Fig. 3.5-(b) and an elliptic curve of the bubble interface at each quadrant was determined by the intercept coordinates and the reference point.

The same procedure was repeated from the topmost elevation to the bottommost one and cross-section configurations at all elevations were obtained. By accumulating these cross-sections along the elevation, an imaginary bubble was reconstructed and Fig. 3.6 and 3.7 presents an example of the bubble reconstruction result.

3.3.2 Verification of reconstruction technique

The reconstruction method proposed in this study was validated using phantom images created by CAD and its applicability for a deformed bubble was evaluated. The validation was carried out in two steps; one with ellipsoidal phantoms, and the other with more realistically shaped solids.

3.3.2.1 Verification for inclined ellipsoids

For the first step, inclined oblate ellipsoids were used as phantoms for the validation. According to the present visualization, as shown in Fig. 2.9, the generated bubble on the lower half of the horizontal heater has an oblate configuration. Moreover, the bubble is inclined downward from the horizon along the circumference of the heater. Thus, it was required to quantify the potential error of the present reconstruction method with the inclined oblate ellipsoids. Ten

three-dimensional oblate ellipsoids with various sphericities (0.80–0.996) were created by prolonging a sphere in the x-direction and y-direction and they were inclined downward by 20°, as shown in Fig. 3.8. The ranges of the sphericity and the inclination were determined by the preliminary visual observation results. The sphericity is the ratio of the surface area of a sphere (with the same volume as the given ellipsoid) to the surface area of the oblate ellipsoid, and is defined as:

$$\psi = \frac{\pi^{1/3} (6V_p)^{2/3}}{A_0} = \frac{2\sqrt[3]{ab^2}}{a + \frac{b^2}{\sqrt{a^2 - b^2}} \ln \left(\frac{a + \sqrt{a^2 - b^2}}{b} \right)} \quad (3-1)$$

where V_p : volume of an ellipsoid; A_0 : surface area of an ellipsoid; a, b: major and minor axis, respectively, of an ellipsoid.

Then, the ellipsoid was projected onto two-dimensional planes rotating the observation angle (θ) by 15° along the vertical axis from 0° to 90°, as exemplified in Fig. 3.9 with the ellipsoids with sphericities of 0.815 and 0.932. The projected images were used for the image reconstruction and error estimation. Prior to calculating the bubble volume using the stereoscopic method, the monoscopic visualization method was applied to produce reference data for error reduction performance of the proposed method.

In the monoscopic analysis, the cross-section on the x-y plane is assumed to be a circle and the volume of the bubble was calculated by numerical integration from the bottom end to the top. Fig. 3.10-(a) shows the volume error caused by the monoscopic method with respect to the sphericity and the observation angle. A considerable error arose due to the inclination and the estimated error was in the range of -26.7%~33.4%. The best result was obtained with the observation angle

of 45° . This result demonstrates that the monoscopic method may cause a significant error in estimating a volume of considerably deformed bubble.

Afterwards, the same procedure was repeated with the stereoscopic analysis. For this, four pairs of images were used with observation angles of $(0^\circ, 90^\circ)$, $(15^\circ, 105^\circ)$, $(30^\circ, 120^\circ)$, and $(45^\circ, 135^\circ)$. As shown in Fig. 3.9-(b), the present stereoscopic observation reduced the volume calculation error significantly into the range of $-1.1\% \sim 4.7\%$. In particular, the error was lower than $\pm 1.1\%$ when the observation directions were in parallel with the semi-principal axes (observation angle pair: 0° and 90°), and the error was enlarged when the ellipsoid was visualized in the diagonal direction between the semi-principal axes (observation angle pair: 45° and 135°). It should be noted that the present experiment takes images from the axial and radial directions of the horizontal rod and they are in parallel with the semi-principal axes of the oblate bubbles. This implies that the present experimental setup and the observation angles can maximize the accuracy of the stereoscopic visualization method.

3.3.2.2 Verification for asymmetric phantom images

As the second validation step of the bubble reconstruction method, four phantom objects with more realistic and arbitrary configurations were analyzed. These objects, which were proposed by Kim et al. (2011) for their bubble

condensation rate analysis, are no longer oblate ellipsoid and as such, they have different lengths of semi-principle axes, as presented in Fig. 3.11. Figure 3.12-(a) shows the volume prediction results using the monoscopic image reconstruction method, which indicate significant discrepancy with the volumes of the phantoms depending on their shapes. The estimated error is in the range of $-44.3\%\sim 81.2\%$. This result clearly shows the limitation of the monoscopic image processing technique for a deformed bubble on an inclined surface. Following this, the stereoscopic observation method was applied and two images obtained from two perpendicular angles were used for the object reconstruction. In total, six pairs of images were used, which were obtained with observation angles of $(0^\circ, 90^\circ)$, $(15^\circ, 105^\circ)$, $(30^\circ, 120^\circ)$, $(45^\circ, 135^\circ)$, $(60^\circ, 150^\circ)$, and $(75^\circ, 165^\circ)$. The volume prediction result was remarkably improved and it has an error range of $-0.6\%\sim 18.0\%$. In addition, it was found that the error can be reduced largely if the two images required for the stereoscopic reconstruction were taken in parallel with the major and minor axes of an object cross-section (observation angle pair: 0° and 90°). For this case, the volume prediction error is in the range of $-0.7\%\sim 0.6\%$. In our bubble visualization, the observation angles in parallel with the major and minor axes were selected and therefore, it was concluded that the present experimental setup and the observation angles are sufficiently optimized for the stereoscopic visualization method.

3.4 Measurement results

This experiment were conducted under the conditions similar to that of natural convection boiling in PAFS. As represented in Table 3.1, the bulk velocity of the experiment ranged from 11.2 to 27.6 mm/s and wall heat flux ranged from 26 to 66 kW/m², which is in the nucleate boiling regime on the boiling curves. The wall heat flux was determined to observe the single bubble behavior and avoid the damage of the heater. The artificial cavity on the heater is located at a specific angle by rotating the tube heater in the range of 0-180° from the bottom of the heater. Although there were differences depending on the experimental conditions, the bubble frequency was in the range of 20-50 Hz in most experimental conditions. Since the data acquisition took 5 seconds, about 100-250 bubbles were collected in each experimental condition to obtain the representation value.

Figures 3.13, 14 and 15 show the average volume transients of bubbles generated at 135°, 45° and 23° nucleation sites, respectively. The volume transient of bubble generated at the 135° nucleation site is simpler than the other cases, since bubbles generated on upper half of the tube heater do not slide but detached from the heating surface after short growth. When the bubble is attached on the heating surface, it grows rapidly. After that, the growth is decelerated gradually with decreasing the contact diameter, and finally the volume is held nearly constant with the lift-off.

On the other hands, bubbles, generated on the lower half such as the 45° and 23° nucleation sites, slide the heating surface after the growth on the nucleation

site. While sliding along the heating surface, the bubble grows gradually through the phase change of superheated liquid near the bubble, as shown in Figs. 3.14 and 15. The average lift-off diameter of 23° cases is larger than that of 45° cases, since bubble generated at lower site has longer sliding length.

As represented in Fig. 3.16, the volume transients of sliding bubble are closely related with the contact diameter between the bubble and heating surface. The growth rate of bubble, the variation in bubble volume, changes sensitively and proportionally to the contact diameter. Thus, in order to predict the bubble volume transient, the contact area should be considered as one of the key parameters, and it is discussed in Chapter. 5.

The bubble frequency is related to the bulk liquid velocity and heat flux as presented in Fig. 3.17. If the bulk liquid velocity is relatively fast, it causes more frequent bubble departures from the nucleation site, so the bubble frequency increases. On the other hand, higher heat flux makes growth rate faster, and it also causes more frequent bubble departures by increasing contact pressure force, which is the reaction force against internal pressure of bubble to the contact area. The detailed definitions of the forces are explained in following section. Meanwhile, the bubble velocity increases continuously during the sliding, and generally has higher value with faster bulk liquid velocity, as shown in Fig. 3.18.

Table 3.1 Test matrix.

3mm heater	11.2mm/s (U013)	22.4mm/s (U026)	27.6mm/s (U032)
0deg (A000)		W3A000U026Q026 W3A000U026Q030 W3A000U026Q049 W3A000U026Q066	
23deg (A023)	W3A023U013Q026 W3A023U013Q030 W3A023U013Q049 W3A023U013Q066	W3A023U026Q026 W3A023U026Q030 W3A023U026Q049 W3A023U026Q066	W3A023U032Q026 W3A023U032Q030 W3A023U032Q049 W3A023U032Q066
45deg (A045)	W3A045U013Q026 W3A045U013Q030 W3A045U013Q049 W3A045U013Q066	W3A045U026Q026 W3A045U026Q030 W3A045U026Q049 W3A045U026Q066	W3A045U032Q026 W3A045U032Q030 W3A045U032Q049 W3A045U032Q066
90deg (A090)		W3A090U026Q026 W3A090U026Q030 W3A090U026Q049	
135deg (A135)	W3A135U013Q026 W3A135U013Q030 W3A135U013Q049 W3A135U013Q066	W3A135U026Q026 W3A135U026Q030 W3A135U026Q049 W3A135U026Q066	W3A135U032Q026 W3A135U032Q030 W3A135U032Q049 W3A135U032Q066
180deg (A180)	W3A180U013Q049 W3A180U013Q066	W3A180U026Q049 W3A180U026Q066	W3A180U032Q049 W3A180U032Q066

- W
: width of heating strip; A: angle of the nucleation site from the bottom of the bottom; U: bulk liquid velocity, Q: heat flux.

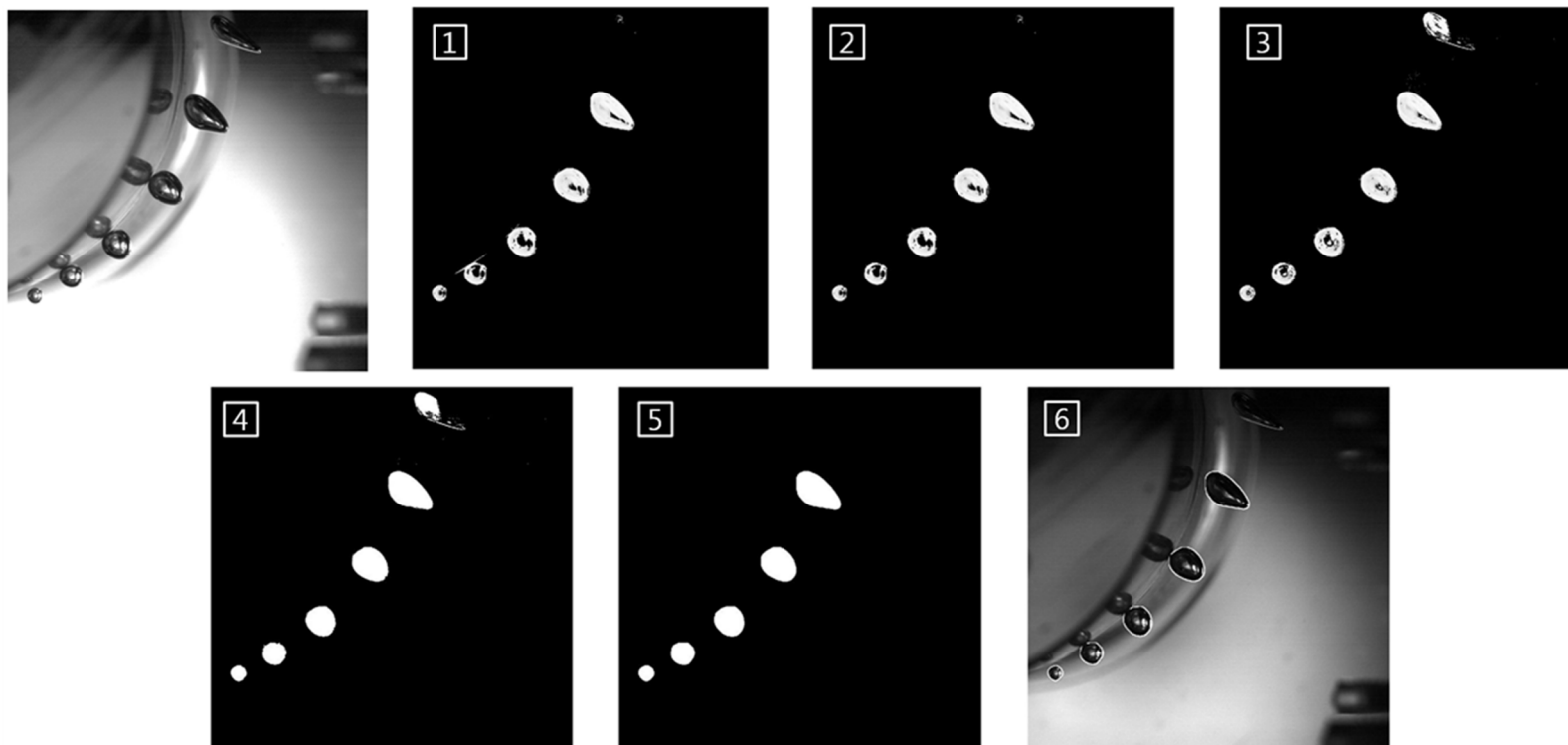


Figure 3.1 Image processing procedures for the phase separation of axial image.

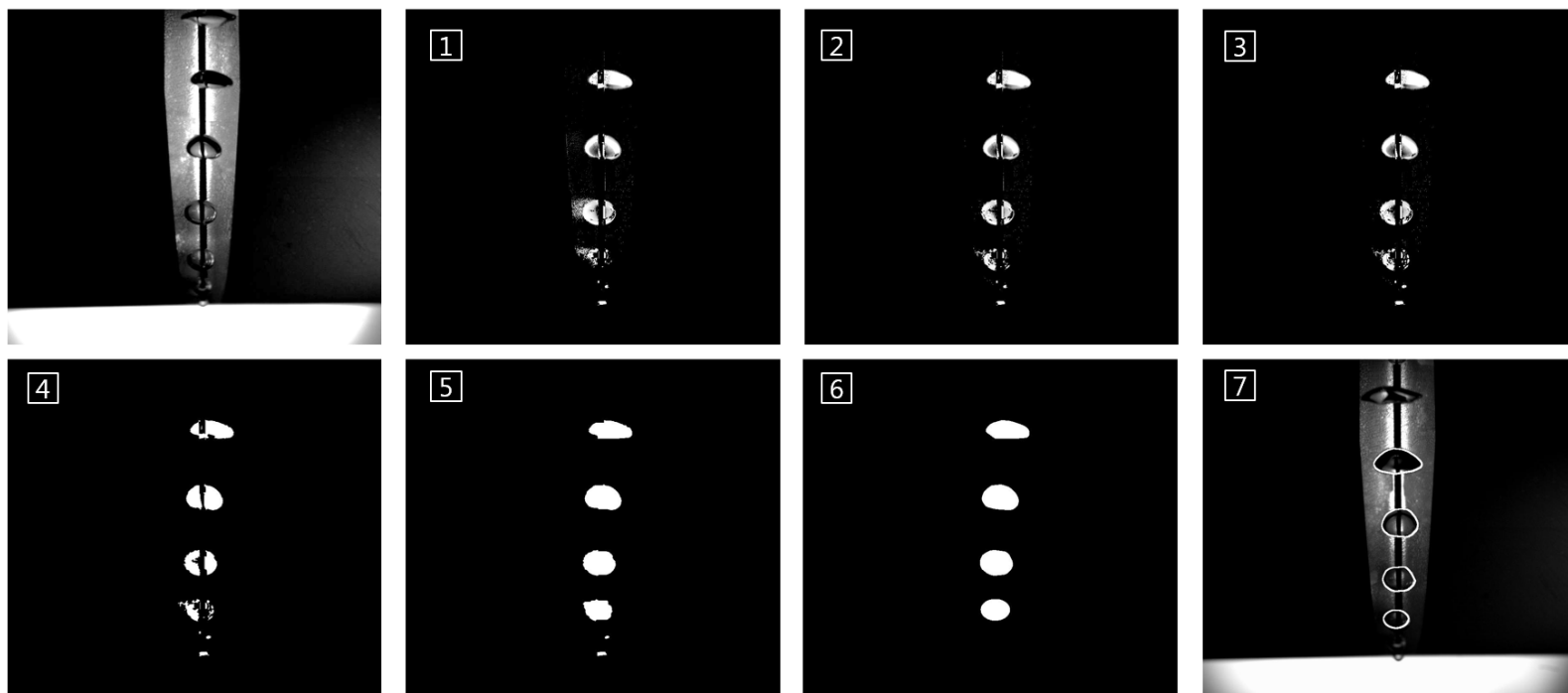


Figure 3.2 Image processing procedures for the phase separation of radial image.

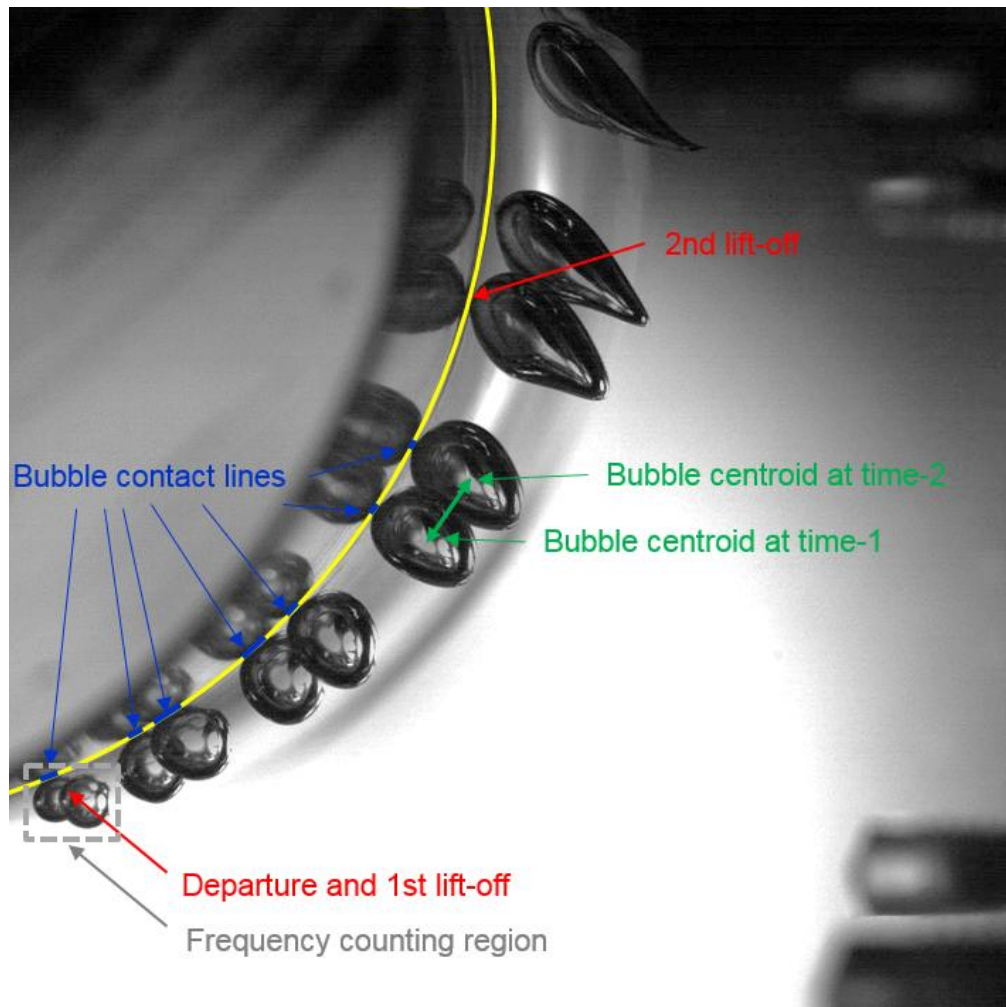


Figure 3.3 Definition of bubble parameters: bubble frequency, contact length, lift-off, velocity.

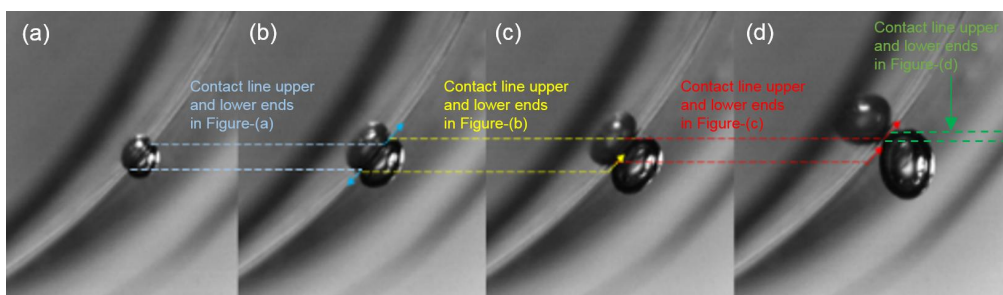


Figure 3.4 Bubble departure identification.

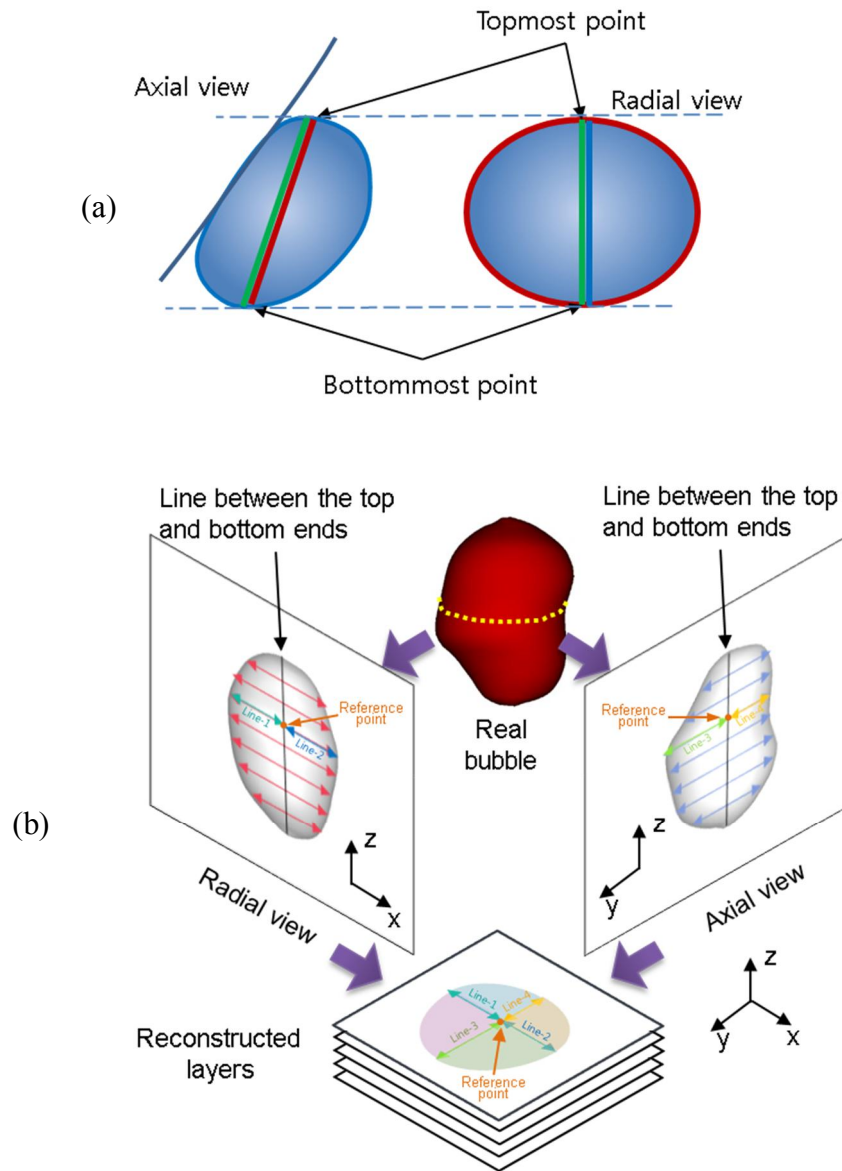


Figure 3.5 Procedure of the cross-section accumulation: (a) line connection between the top and bottom points, (b) cross-section reconstruction.

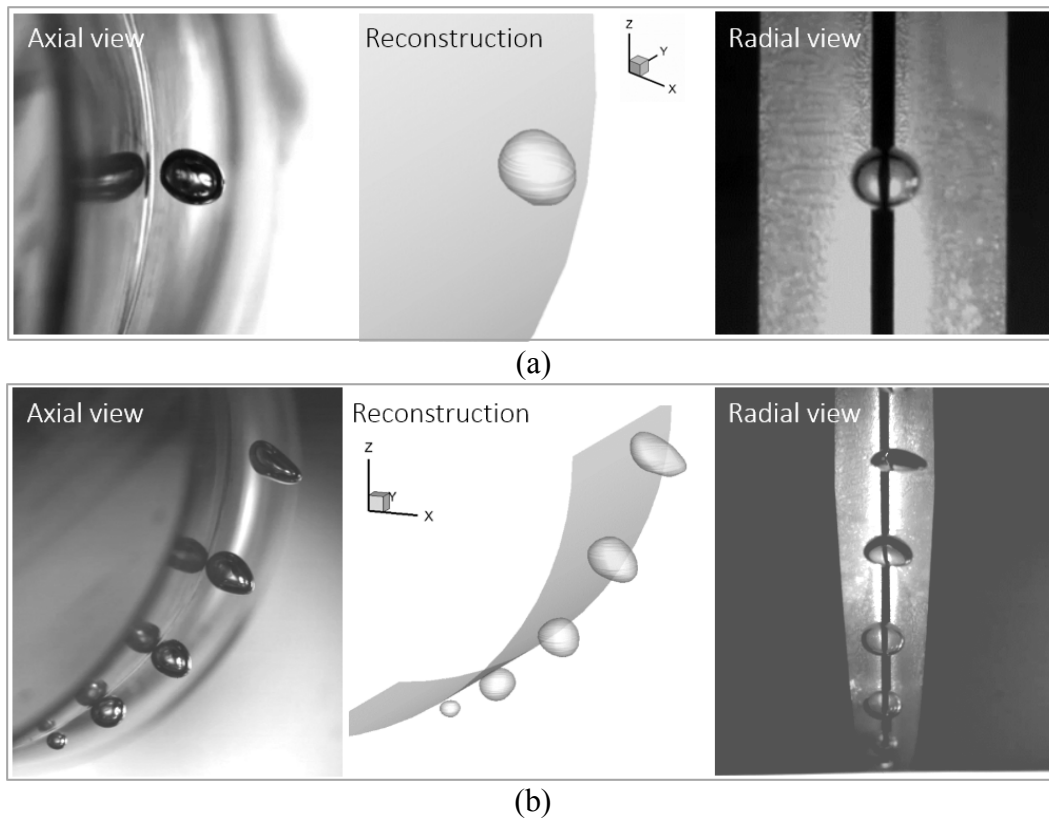


Figure 3.6 Synchronized axial image (left), reconstruction result image (middle) and synchronized radial image (right): (a) 90° nucleation location, (b) 23° nucleation location.

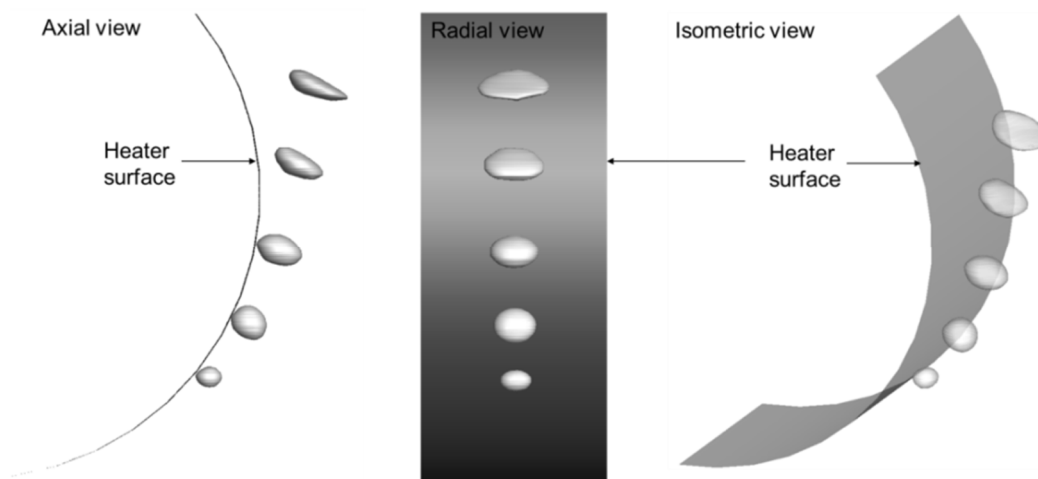


Figure 3.7 Reconstruction result of bubbles in various views.

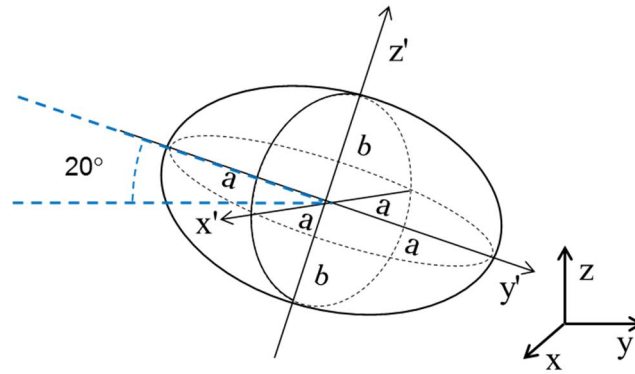


Figure 3.8 Inclined oblate ellipsoid based on configuration of observed bubble.

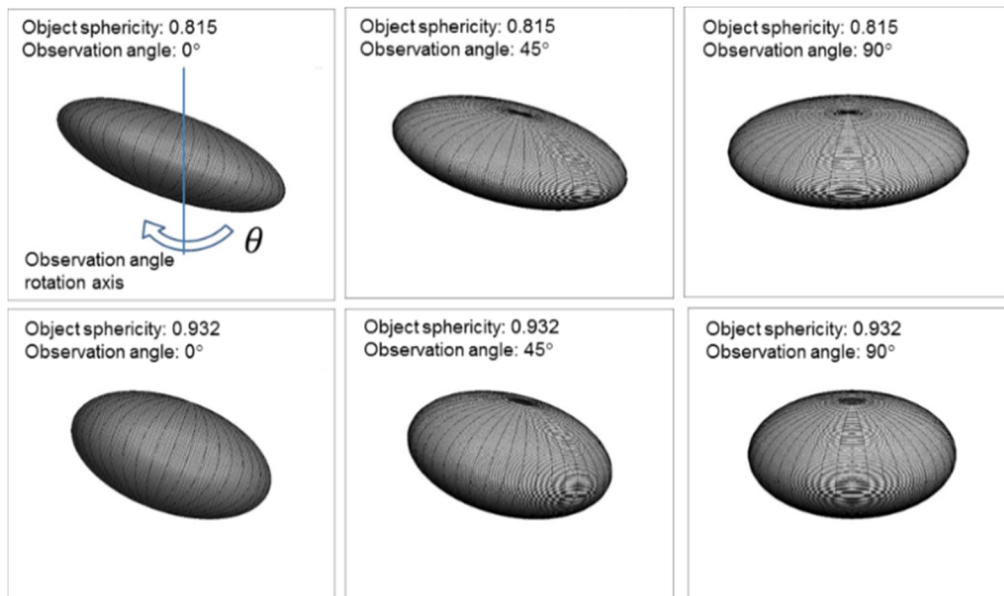


Figure 3.9 Examples of ellipsoids by observation angles.

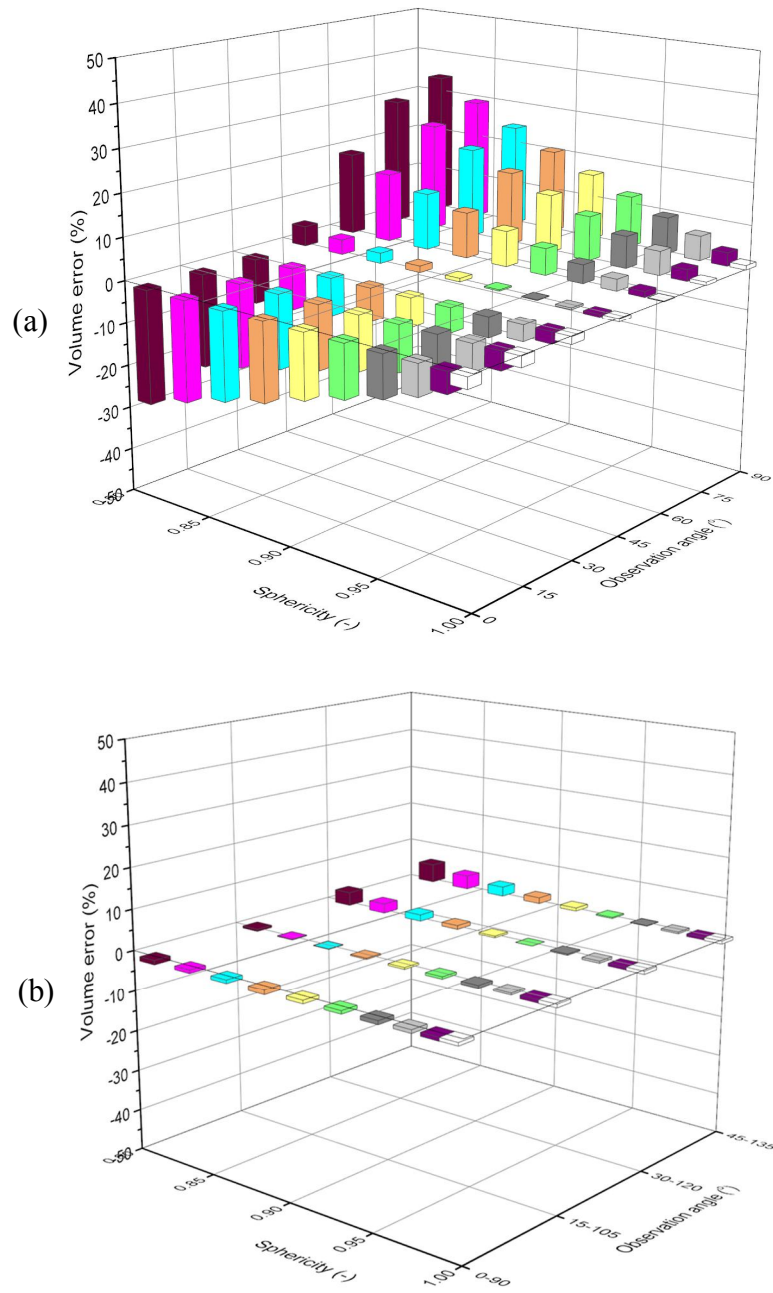


Figure 3.10 Verification of reconstruction methods for inclined ellipsoids:
(a) Errors of monoscopic reconstruction by sphericity and observation angle,
(b) Errors of stereoscopic reconstruction by sphericity and observation angle.

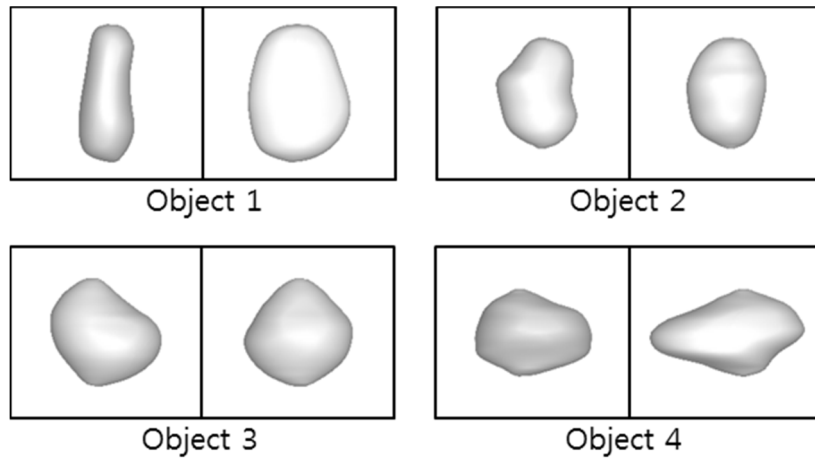


Figure 3.11 Asymmetric phantom objects (observation angle: 0° , 90°).

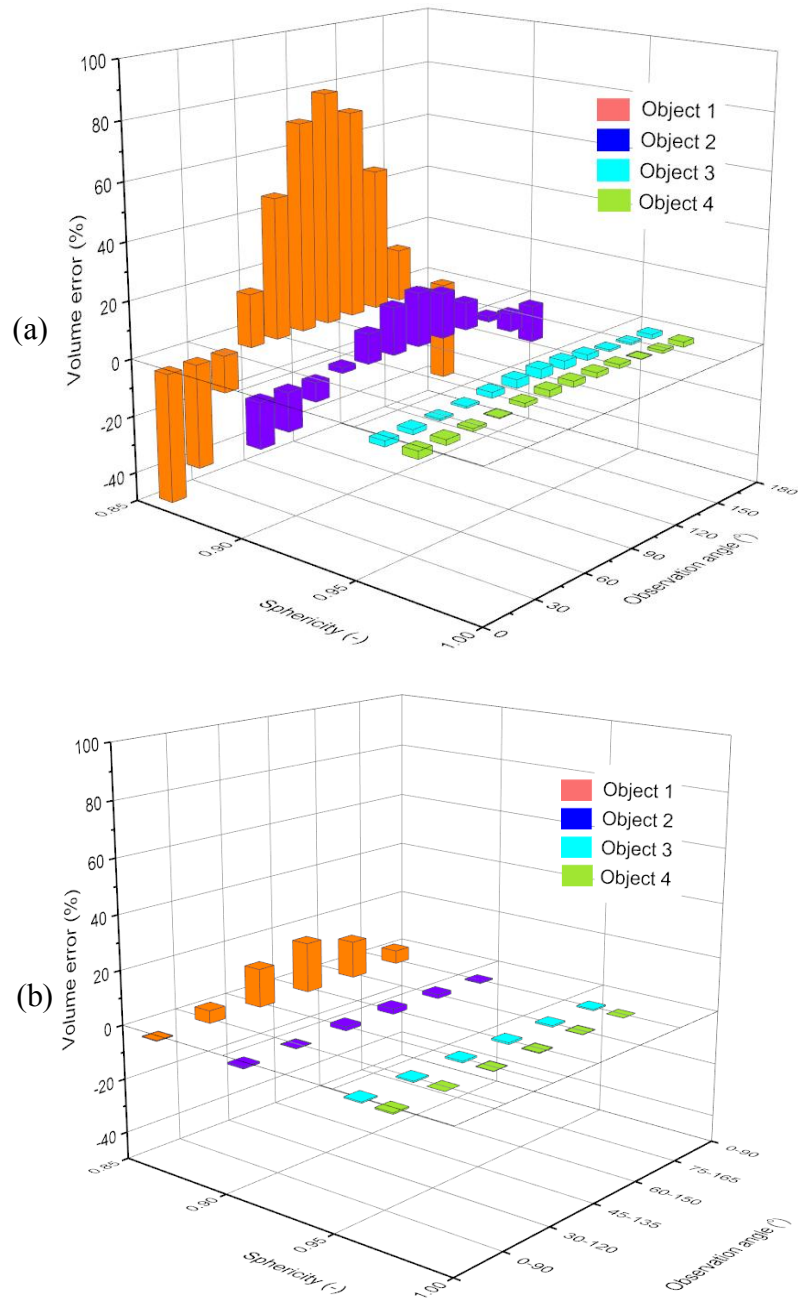


Figure 3.12 Verification of reconstruction methods for asymmetric phantom images: (a) Errors of monoscopic reconstruction by sphericity and observation angle, (b) Errors of stereoscopic reconstruction by sphericity and observation angle.

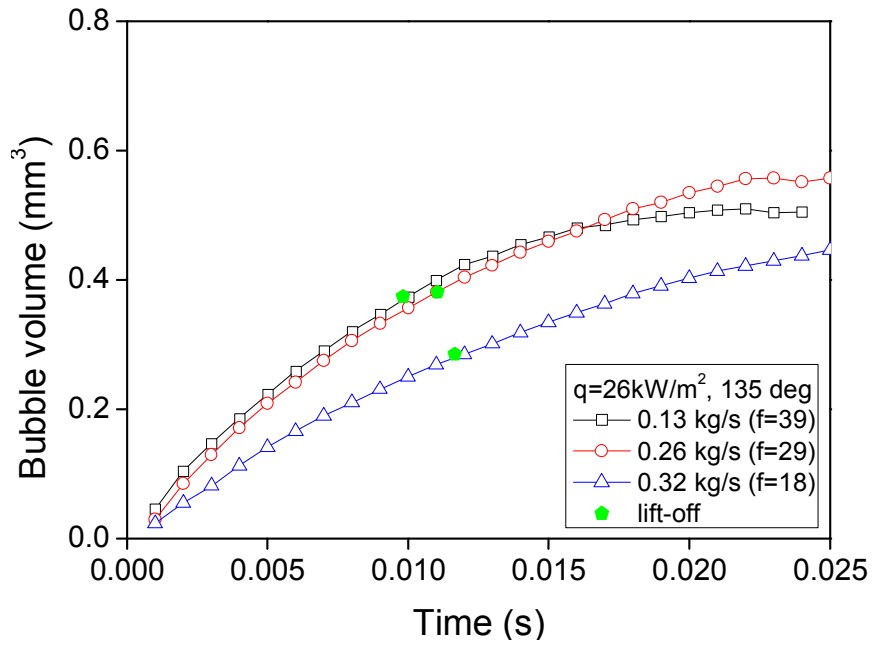


Figure 3.13 Measured bubble volume transient with various bulk liquid velocity of 135° nucleation location.

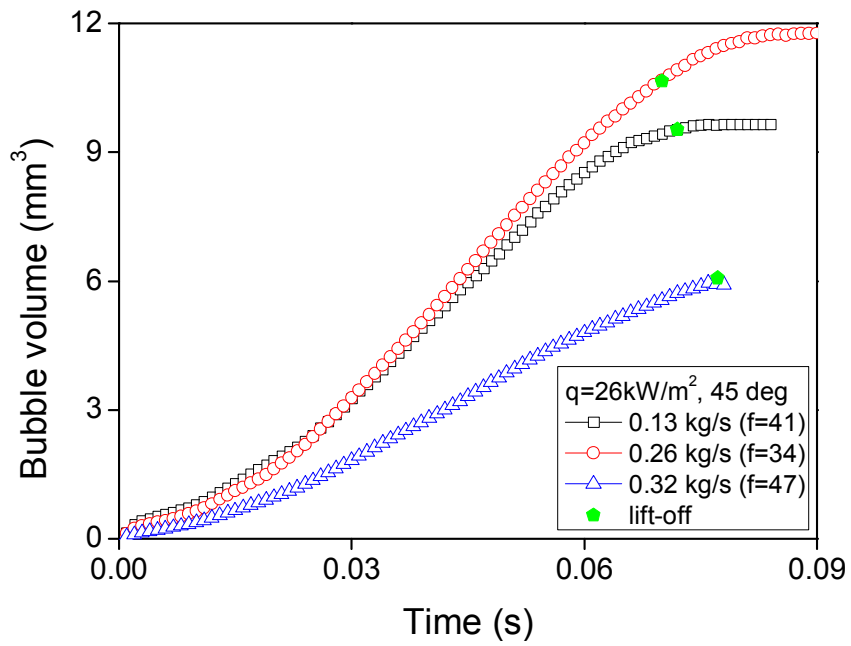


Figure 3.14 Measured bubble volume transient with various bulk liquid velocity of 45° nucleation location.

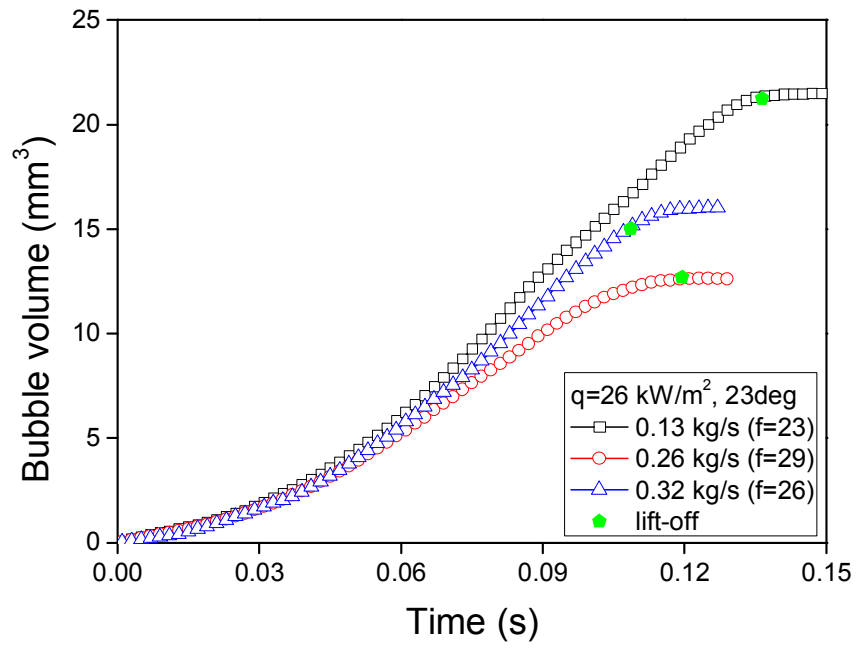


Figure 3.15 Measured bubble volume transient with various bulk liquid velocity of 23° nucleation location.

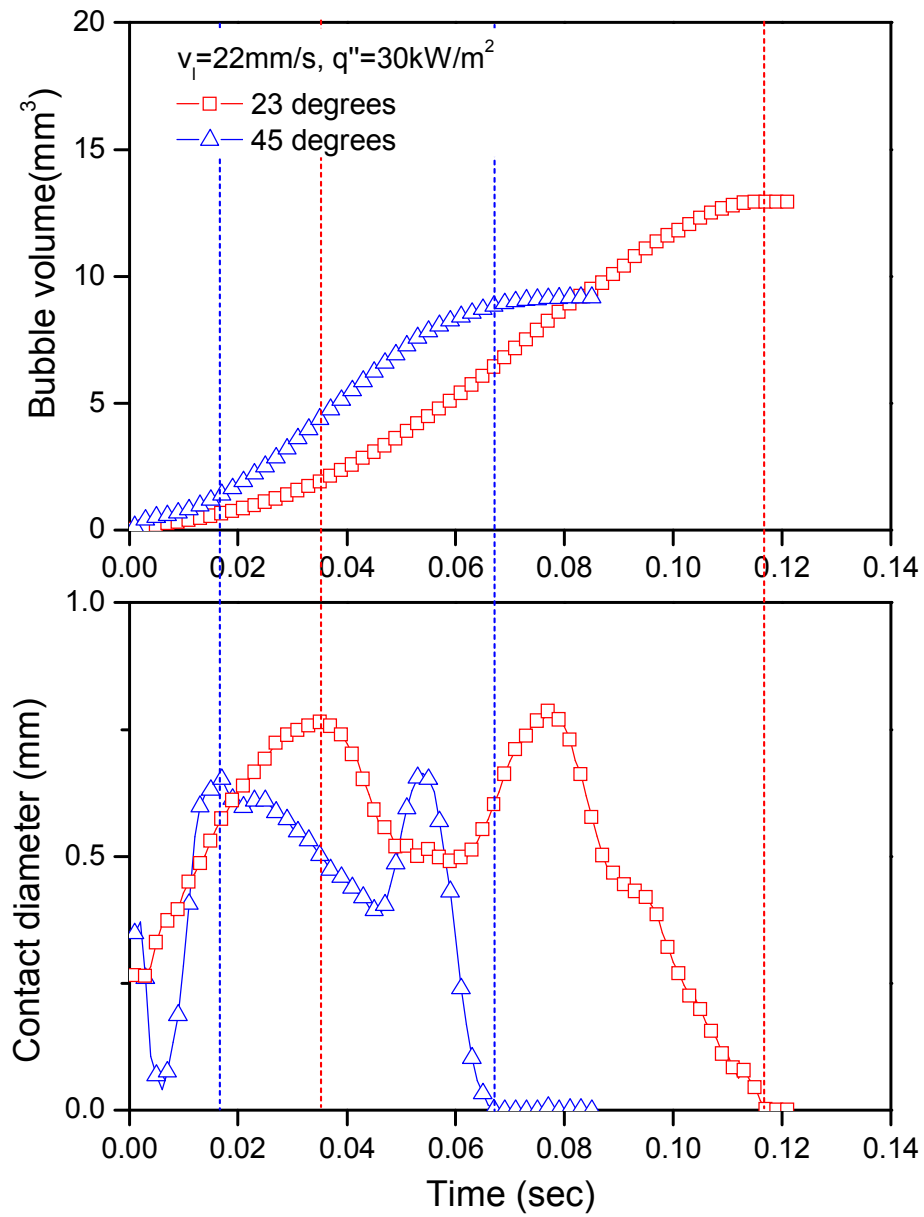


Figure 2.16 Relation between transients of bubble equivalent diameter and contact line length.

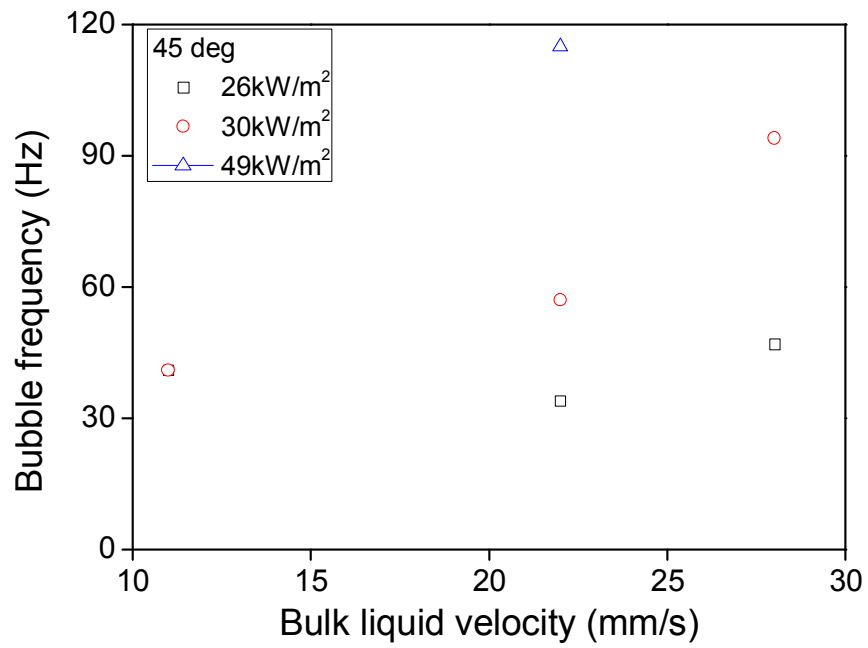


Figure 3.17 Measured bubble frequency with various heat flux of 45° nucleation location.

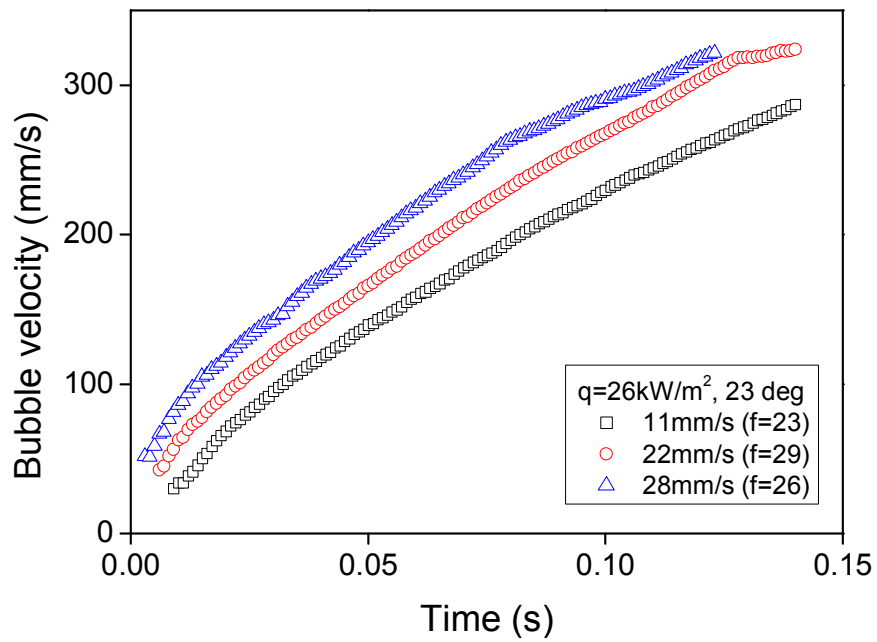


Figure 3.18 Measured bubble velocity with various bulk liquid velocity of 23° nucleation location.

Chapter 4.

Force Balance Analysis

4.1 Force balance model for a sliding bubble on the horizontal tube

In previous studies, in order to predict the sliding bubble behavior, the forces acting on a sliding bubble were analyzed using a force balance model. The departure and lift-off of the bubble are defined as moments of the off-balance in parallel and normal directions, respectively. In this study, the force balance model was improved for a sliding bubble on the horizontal tube by considering direction of forces and additional force based on Klausner model (Klausner et al., 1993).

The Klausner model is inappropriate for a sliding bubble on the horizontal tube since the model is expressed in the XY coordinates. Thus, the coordinate system of the improved force balance model in this study is modified to the cylindrical coordinates to express the circular sliding motion of a bubble. This model can consider continuously changing directions of the forces during sliding. The forces included in the force balance model are explained below and depicted in Fig. 4.1.

- Buoyancy (F_b)

It is a force caused by density difference between water and vapor, acting in the opposite direction of gravity.

- Surface tension force (F_s)

The surface tension force is applied by the heating surface to the bubble, interrupting the lift-off of sliding bubble.

- Quasi-steady drag (F_{qs})

The drag force is caused by velocity difference between the sliding bubble and surrounding liquid.

- Lift force (F_L)

The lift force is caused by the local liquid velocity gradient and relative velocity of bubble and liquid. When a bubble slides near the wall, the shear velocity gradient of liquid induces difference of the pressure and shear stress between the top and bottom of the bubble. The force pushes the bubble from the wall (Rousselet, 2014).

- Contact pressure force (F_{cp})

It is a force given to a bubble in a reaction to the internal pressure of the bubble acting on the contact area. The radius of curvature of the bubble at the heater surface, r_r , is defined in order to estimate the internal pressure of bubble.

- Hydrodynamic pressure force (F_h)

If a bubble contacts to the wall, the shape of the bubble is asymmetric in vertical direction, which means that the bottom of the bubble is flatter than the top. The force is induced by the difference of hydrodynamic pressure between the top and bottom due to the asymmetric shape.

- Added mass force (F_{am})

This force means the added inertia to accelerated sliding bubble, since the accelerated bubble must move with some volume of surrounding liquid together. Consequently, it interrupts the acceleration of sliding bubble. The acceleration includes not only the acceleration of bubble centroid but also growth acceleration (Thorncroft et al., 2001).

- Dynamic pressure force (F_{dp})

The force is the pressure force caused by the direction change of bulk liquid by the obstacle such as the horizontal tube.

The forces acting on a sliding bubble are considered in cylindrical coordinate force balance analysis. The θ -directional force balance analysis is used for estimation of local liquid velocity of surrounding liquid, and that of r-direction is used for prediction of lift-off moment and estimation of local liquid velocity gradient. It will be discussed in detail in the following section.

4.2 θ -directional force balance analysis

The θ -directional force balance analysis was conducted to estimate the local velocity of liquid near the bubble that could not be measured from experimental observations. The θ -directional force balance model consists of the forces described as below and depicted in Fig. 4.2-(a).

Buoyancy	$F_{b\theta} = (\rho_l - \rho_v)gV_b \sin\theta_b$	(4-1)
----------	--	-------

$$\begin{aligned}
F_{s\theta} &= - \int_0^\pi d_w \sigma \cos \gamma \cos \phi d\phi \\
\text{Surface tension force} & \\
&\sim d_w \sigma \frac{\pi(\alpha - \beta)}{\pi^2 - (\alpha - \beta)^2} [\sin \alpha + \sin \beta]
\end{aligned} \tag{4-2}$$

$$\begin{aligned}
\text{Stagnation force} & \\
F_{st\theta} &= \rho_l V_{bulk}^2 A \sin \theta_b
\end{aligned} \tag{4-3}$$

$$\begin{aligned}
\text{Quasi-steady drag} & \\
F_{qs} &= -\frac{1}{2} C_D \rho_l (v_l - v_b)^2 A
\end{aligned} \tag{4-4}$$

$$\begin{aligned}
\text{Added mass force} & \\
F_{am\theta} &= -\frac{1}{2} \rho_l V_b \left(2v_r \omega + R \frac{d\omega}{dt} \right) \\
&\quad + 2A \rho_l (v_l - v_b) \dot{r}_b
\end{aligned} \tag{4-5}$$

- | | |
|--|--------------------------------------|
| - ρ : density; | V_b : volume of a bubble; |
| θ : angle of the bubble centroid; | C_D : coefficient of drag; |
| A : cross section of a bubble; | d_w : contact diameter; |
| σ : surface tension; | α : upstream contact angle; |
| β : downstream contact angle; | r : bubble radius; |
| v_l : local liquid velocity; | v_b : velocity of bubble centroid; |
| V_{bulk} : bulk liquid velocity; | ω : bubble angular velocity; |
| v_r : radial velocity of bubble; | |
| R : distance between centroids of bubble and tube. | |

The coefficient of Quasi-steady drag force, C_D , is defined as:

$$C_D = 0.44 C_{deform} \left(1 - \left(\frac{r_b}{2d} \right)^3 \right)^{-2} \tag{4-6}$$

It considers the deformation effect that the cross section of bubble is enlarged by

the drag, and the wall effect proposed by Van der Geld (2002). The deformation coefficient, C_{deform} , was defined as the ratio of the maximum cross-sectional area to the equivalent cross-sectional area of the bubble.

As presented in the above equations, most of the bubble parameters required for calculation of the forces can be measured by the experiment. However, only the local velocity of liquid near the bubble, which is not able to be measured in an experiment, remains unknown. At that time, the sum of θ -directional forces determines the θ -directional acceleration of bubble centroid as represented below.

$$\rho_v V_b \left(2v_r \omega + R \frac{d\omega}{dt} \right) = \Sigma F_\theta \quad (4-7)$$

Thus, the local liquid velocity can be estimated by calculating the equation with experimental data, and the results of those are presented in Fig. 4.3.

The estimated local liquid velocities show reasonable trends according to the experimental conditions, which is that the local liquid velocity is proportional to the bulk liquid velocity and bubble frequency. The bubble velocity and frequency are important parameters to determine the local liquid velocity, since the bubble, sliding faster than bulk liquid, accelerates the local velocity of liquid near a sliding bubble. When the bulk liquid velocity is fast, sliding velocity of bubble is also fast, and it can accelerate the local liquid rapidly. On the other hand, when the bubble frequency is high, the distance between two consecutive bubbles is short, and the following bubble enters quickly in wake region created by the preceding bubble. Therefore, the local liquid velocity with higher bubble frequency is faster than that with lower bubble frequency.

4.3 R-directional force balance analysis

The r-directional force balance analysis was conducted to predict the lift-off of sliding bubble and to deduce the local velocity gradient of liquid. The forces acting in this direction are represented below and Fig. 4.2-(b).

$$\text{Lift force} \quad F_L = \frac{1}{2} \rho_l V_b \frac{dv_l}{dr} |v_l - v_b| \quad (4-8)$$

$$\text{Contact pressure force} \quad F_{cp} = \frac{\pi d_w^2}{4} \frac{2\sigma}{r_r} \quad (4-9)$$

$$\text{Hydrodynamic pressure force} \quad F_h = \frac{1}{2} \frac{9}{4} \rho_l v_l^2 \frac{\pi d_w^2}{4} \quad (4-10)$$

$$\begin{aligned} \text{Added mass force} \quad F_{amr} = & -\frac{1}{2} \rho_l V_b \left(\frac{d^2 R}{dt^2} - R \omega^2 \right) \\ & + 2A \rho_l (v_r) \dot{r}_b \end{aligned} \quad (4-11)$$

$$\text{Buoyancy} \quad F_{br} = -(\rho_l - \rho_v) g V_b \cos \theta_b \quad (4-12)$$

$$\begin{aligned} \text{Surface tension force} \quad F_{sr} = & - \int_0^\pi d_w \sigma \sin \gamma d\phi \\ \sim & - d_w \sigma \frac{\pi}{(\alpha - \beta)} [\cos \beta - \cos \alpha] \end{aligned} \quad (4-13)$$

Stagnation force
$$F_{str} = \rho_l V_{bulk}^2 A \cos \theta_b \quad (4-14)$$

- r_r : radius of curvature of the bubble at the heater surface

Similar to θ -directional force balance analysis, most of the bubble parameters, required for force calculations, can be obtained from the experiment. In addition, the local liquid velocity, estimated in θ -directional analysis, is used instead of the experimental measurement. The r-directional force balance model also has the only unknown parameter, the local velocity gradient of liquid. In the Klausner model, linear velocity gradient of liquid was assumed, since it was based on the experiment with refrigerant R113, highly viscous liquid. On the other hand, the working fluid of the present experiment is the saturated water that lower viscosity fluid than R113. Therefore, the local velocity gradient of liquid has to be deduced by the analysis instead of the assumption of linear velocity gradient. Therefore, present study deduces the local velocity gradient of liquid from the r-directional force balance analysis and introduces the correction factor for estimation of velocity gradient such as below equation.

$$\frac{dv_l}{dr} = \frac{v_l}{d} f_c \quad , \quad (4-15)$$

where f_c : velocity gradient correction factor. The correction factor is determined as the optimal value predicting the lift-off location in each experimental condition. The procedures for prediction of the lift-off and decision of the correction factor are as follows.

- The sum of forces acting in radial direction determines the radial acceleration of the sliding bubble. Then, the radial movement of bubble

centroid is driven by the calculated acceleration as below.

$$\rho_v V_b \left(\frac{d^2 R}{dt^2} - R \omega^2 \right) = \Sigma F_r \quad (4-16)$$

$$v_r(t_0 + dt) = \max \left(v_r(t_0) + \frac{d^2 R}{dt^2} dt, 0 \right) \quad (4-17)$$

$$R(t_0 + dt) = R(t_0) + \int_{t_0}^{t_0+dt} v_r(t) dt + \frac{\Delta r_b}{2} \quad (4-18)$$

- Then, the contact diameter is calculated by relation between the distance of bubble centroid from the heating surface and the equivalent radius of bubble such as below equation.

$$d_w(t) = 2(r_b^2 - (R(t) - r_{tube})^2)^{1/2} \quad (4-19)$$

- Repeating this procedure in every time steps, the lift-off can be defined as the moment when the contact diameter becomes zero. The local velocity gradient of liquid can be predicted by comparison of the predicted and experimental lift-off location. Accordingly, the correction factor is deduced in each experimental condition.

The deduced correction factors show declining tendency for liquid velocity such as presented in Fig. 4.4. If the local liquid velocity is slower, the velocity gradient does not deviate significantly from the linear assumption, while the gradient is more gradual with faster liquid. One of the reason is that if the local liquid velocity is slower, the gradient of linear assumption itself is smaller and is not significantly different with actual value such as Fig. 4.5-(a). The other is that the local velocity gradient of the faster liquid at bubble centroid is more gradual, since the velocity gradient is very high near the wall resulting in lower gradient out of the boundary layer as shown in Fig. 4.5-(b).

4.4 Analysis result

Using the measured and estimated bubble parameters, all forces acting on a sliding bubble are calculated quantitatively. Fig. 4.6 represents the results of the analysis. In order to analyze the force balance model, the entire life cycle of single sliding bubble should be observed. So several cases, in which single bubbles slide along the downward heating surface without merged bubbles, were selected for the analysis.

The dominant forces determining bubble behavior vary according to the sliding behavior. During the bubble sliding, surface tension force and contact pressure force are dominant, since the sliding bubble is in contact widely with the surface. Regardless of those, buoyancy and added mass force interrupting the acceleration of the bubble are also significant. Meanwhile as the contact area becomes almost zero at the lift-off moment, the surface tension force and contact pressure force decrease rapidly, but lift force increases with acceleration of sliding bubble. At that time, the buoyancy and added mass force are also dominant. The added mass force is the inertial force of the surrounding liquid near the sliding bubble. It has different meaning depending on the bubble behavior. In the circular motion, it includes a term to prevent acceleration and a term of centrifugal force. During sliding, the term to prevent acceleration is more dominant than the other, since the acceleration determined by sum of forces is fast. However, the term of centrifugal force is more dominant relatively, just before the lift-off, since the angular speed of the liquid increases. This force plays an important role in

determining the lift-off, which is the unique feature of the sliding bubble on the horizontal tube

Fig. 4.7, the example of predicted bubble trajectory, shows that the trajectory tracked by the force balance model matches well with the experimental observation result. The lift-off location and the diameter of every experimental cases can be predicted by the model with under $\pm 5\%$ error as represented in Fig. 4.8. It confirmed that this force balance model is available to predict behavior of a sliding bubble on curved surface such as the horizontal tube.

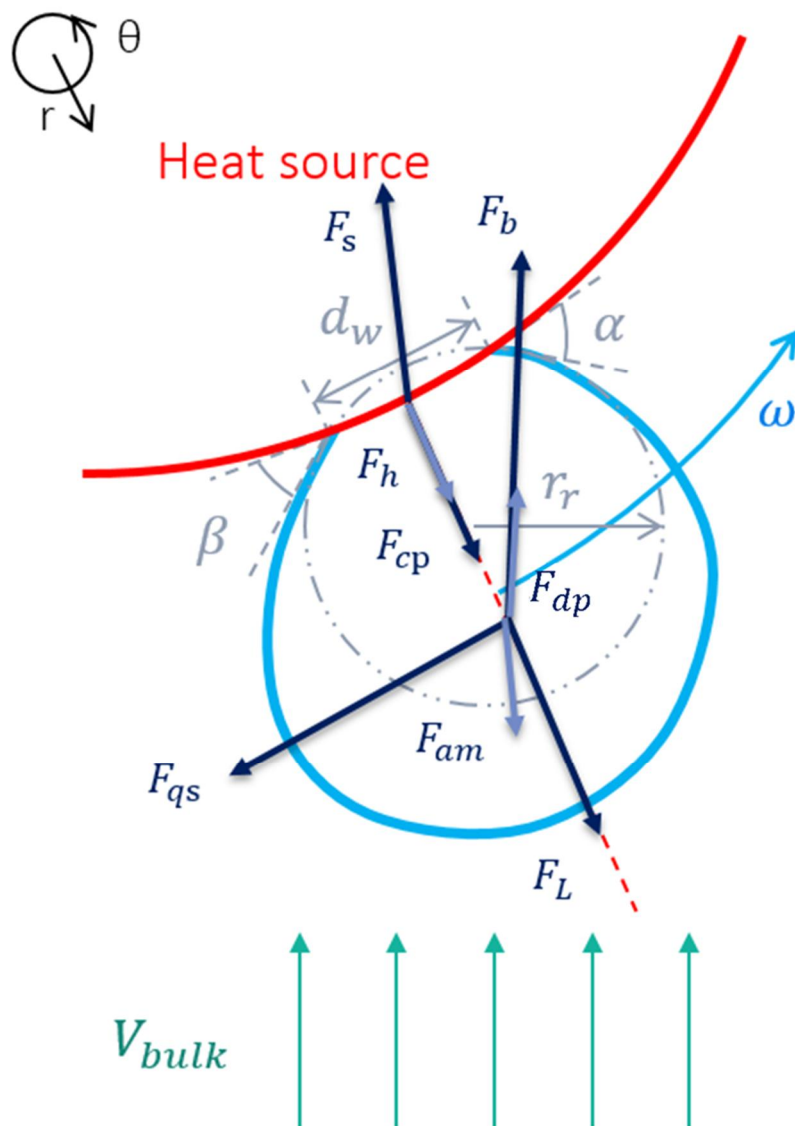


Figure 4.1 Forces acting on a sliding bubble.

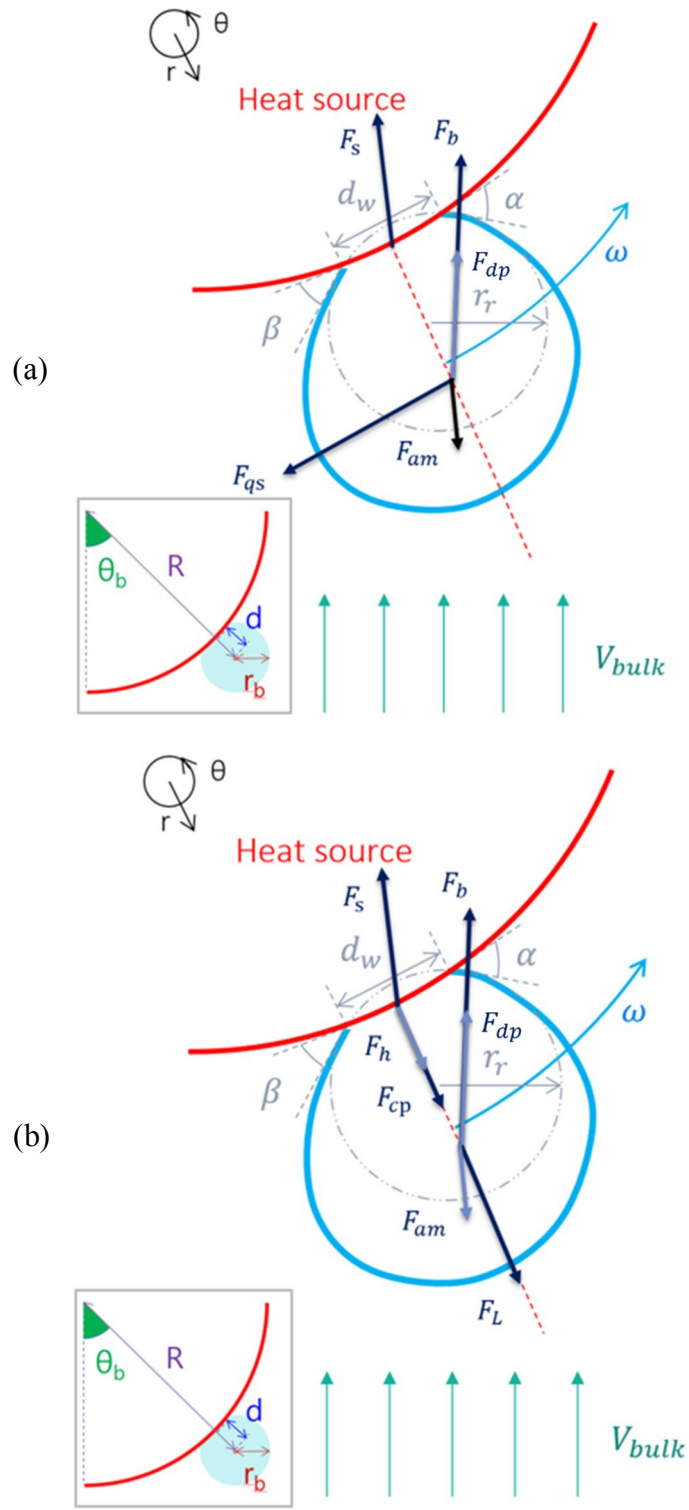


Figure 4.2 Force balance model: (a) in θ -direction, (b) in r -direction.

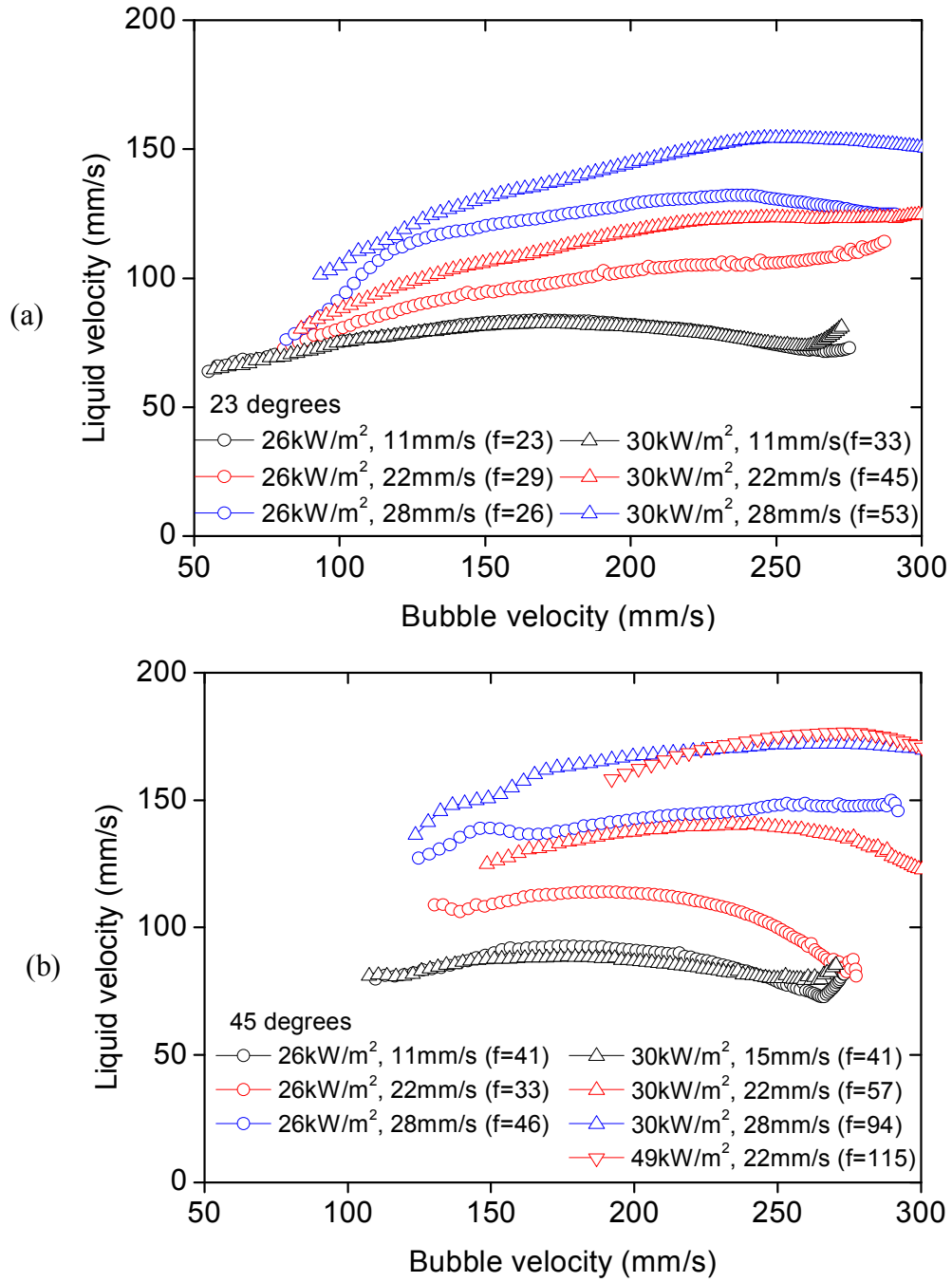


Figure 4.3 Estimated local liquid velocity: (a) 23° nucleation location, (b) 45° nucleation location.

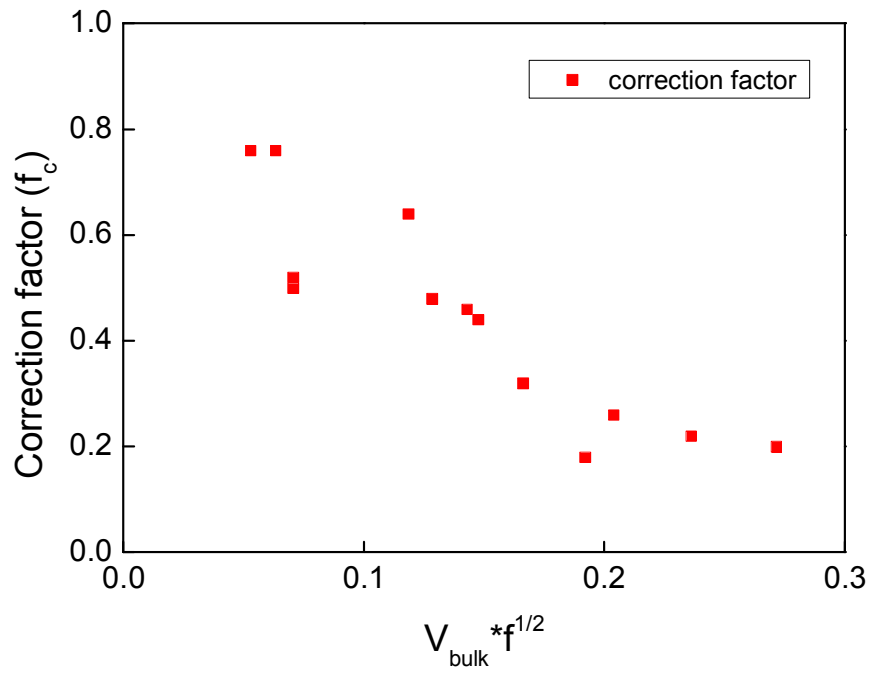


Figure 4.4 Velocity gradient correction factor relative to local liquid velocity.

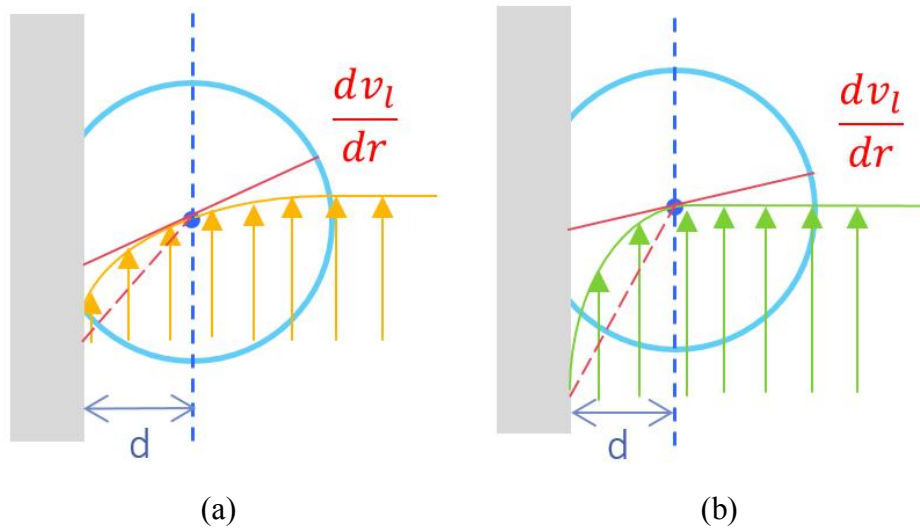
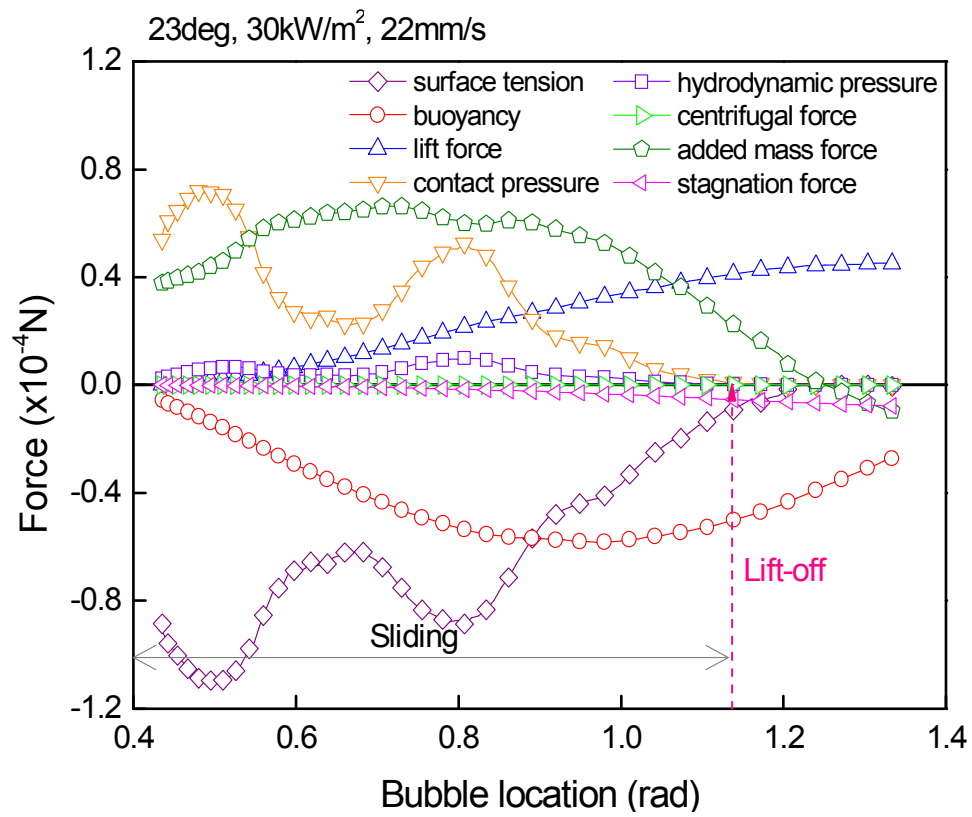


Figure 4.5 Liquid velocity gradient at bubble centroid: (a) slow liquid velocity, (b) fast liquid velocity.



(a)

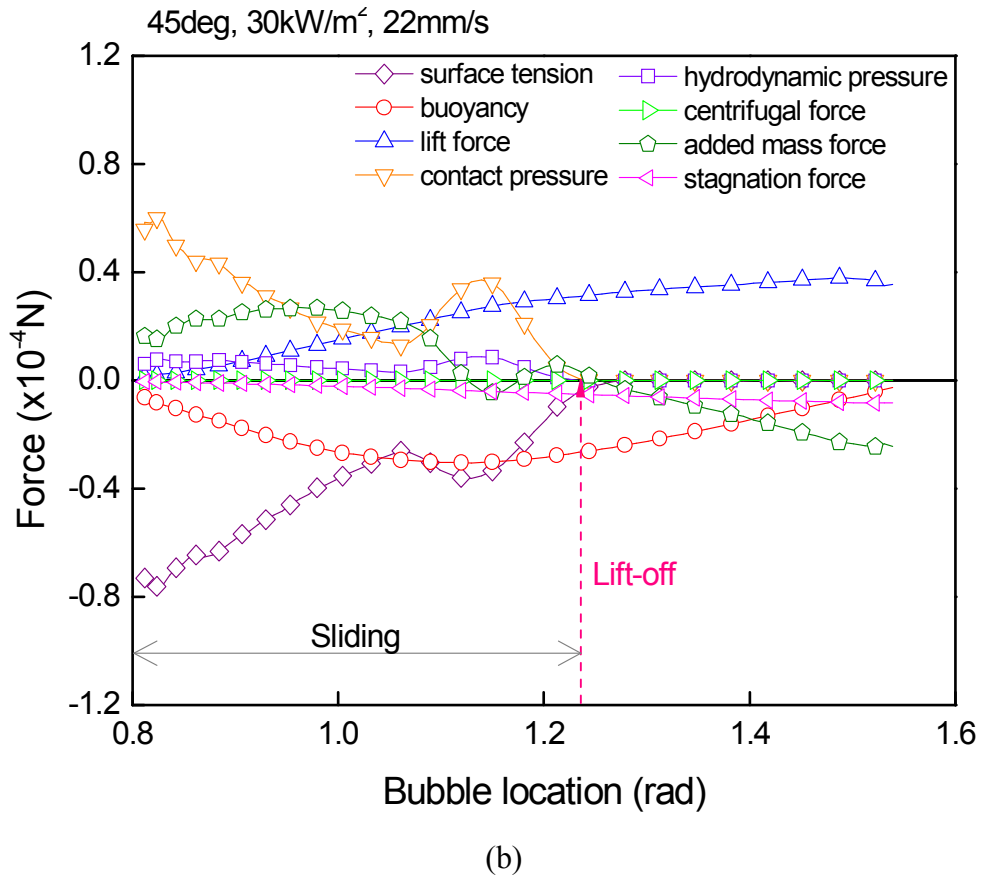


Figure 4.6 Result of radial force balance analysis: (a) 23° nucleation location, (b) 45° nucleation location.

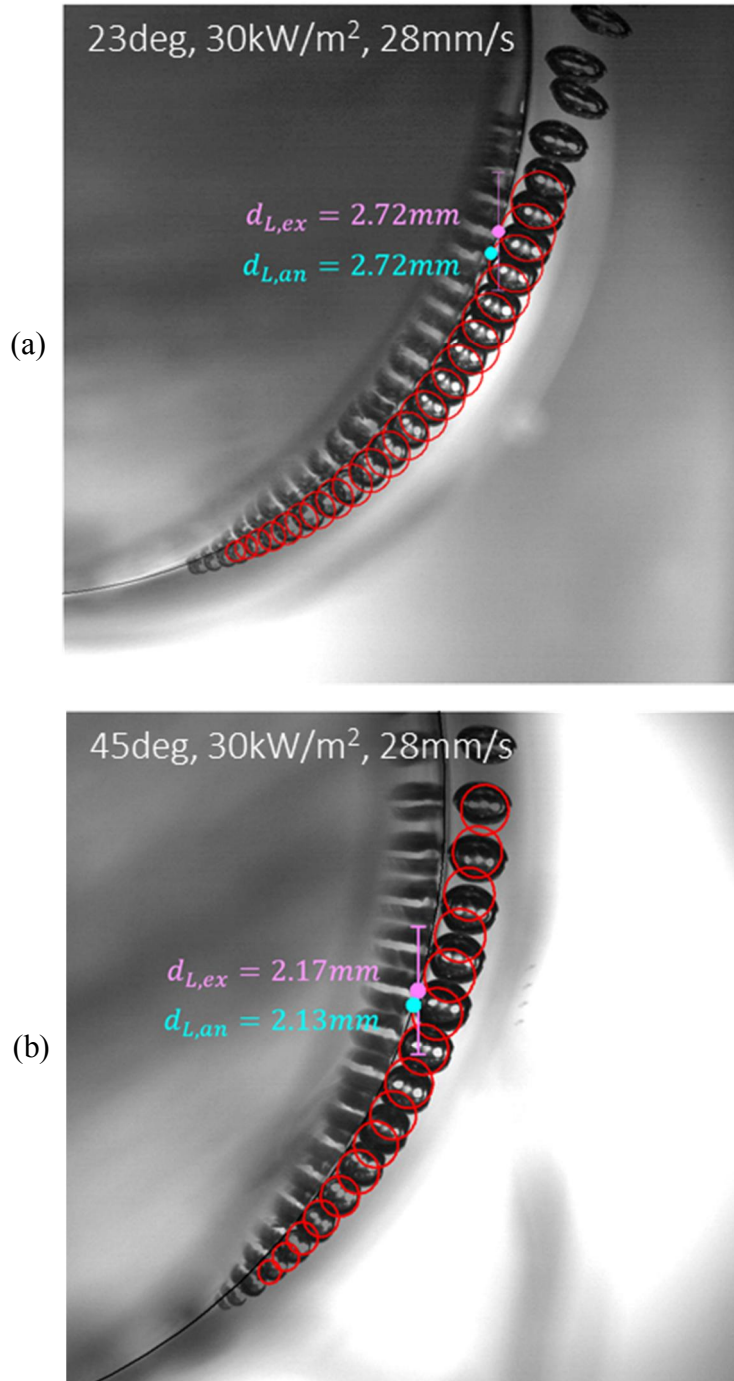


Figure 4.7 Bubble trajectory tracked by the force balance model on overlapped experimental image: (a) 23° nucleation location, (b) 45° nucleation location.

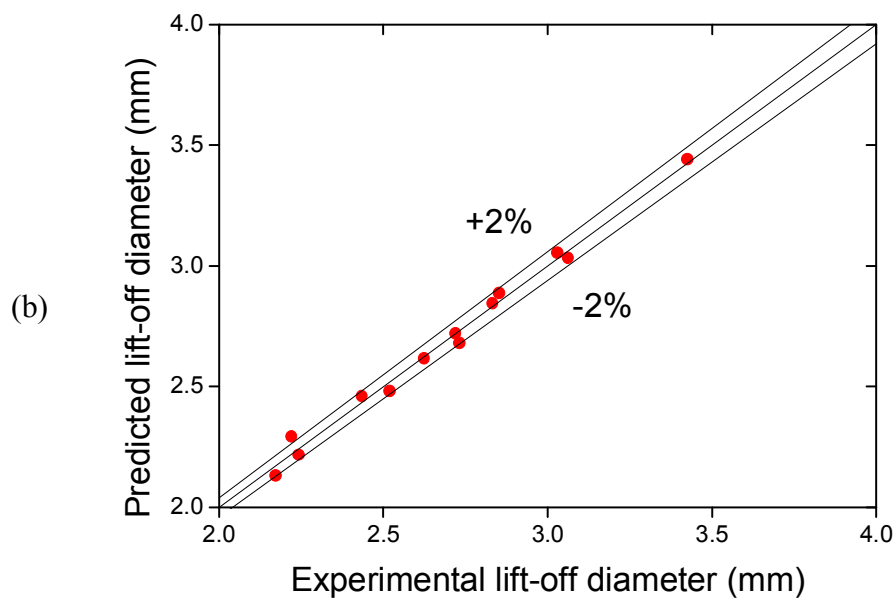
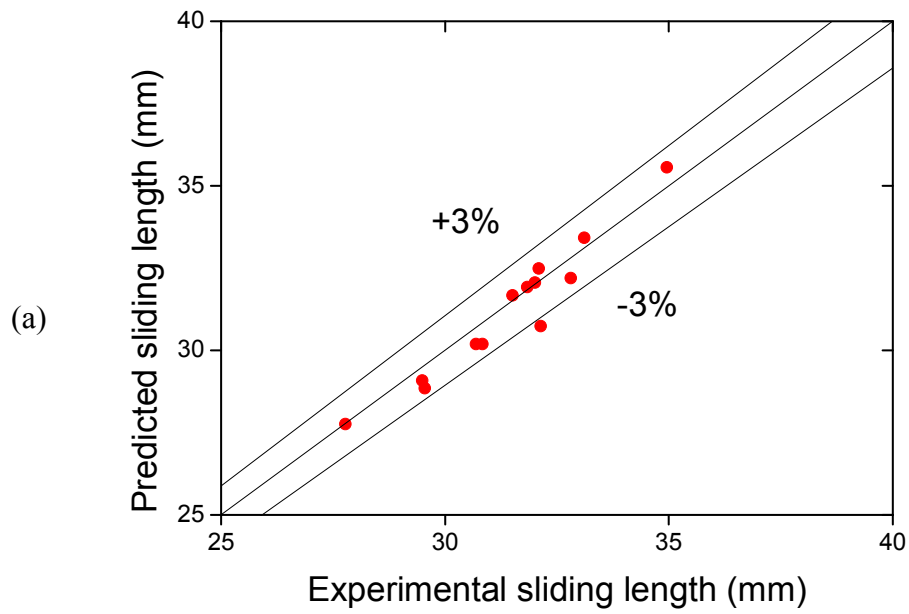


Figure 4.8 Prediction result of the improved force balance model: (a) sliding length, (b) lift-off diameter.

Chapter 5.

Closure of Force Balance Model

5.1 Empirical correlation for bubble behavior parameters

In order to make bubble behavior parameters available for prediction of bubble behavior, various parameters are modeled based on the experimental data. The empirical correlations of each parameter are presented below.

5.1.1 Local liquid velocity

As a result of experimental observation and prediction using the force balance model, the local liquid velocity increases gradually with increasing bubble sliding velocity, and then it converges on a constant. According to this transient, the empirical correlation of local liquid velocity is defined as a function of the bubble velocity. Thus, increasing trend is estimated using a second-polynomial function, and after reaching a specific value, it is modeled as constant like as below equation.

$$v_l = \min(av_b^2 + bv_b + c, d) \quad (5-1)$$

As mentioned before, the increasing rate and overall value of local liquid velocity are closely related to the bulk liquid velocity and the bubble frequency.

Specially, since the tendency of the local liquid velocity was most clearly identified by $V_{bulk}f^{1/2}$, coefficients of the function are determined by fitting the tendency of this experimental parameter as shown in Fig. 5.1 and below.

$$a = -8.062V_{bulk}f^{1/2} - 0.876 \quad (5-2)$$

$$b = -4.608V_{bulk}f^{1/2} + 0.310 \quad (5-3)$$

$$c = -0.180V_{bulk}f^{1/2} + 0.032 \quad (5-4)$$

$$d = -0.434V_{bulk}f^{1/2} + 0.057 \quad (5-5)$$

5.1.2 Bubble deformation coefficient

Deformation of sliding bubble is caused by the relative velocity of bubble and surrounding liquid, and the deformation is intensified gradually during sliding. The deformation coefficient, C_{deform} , was defined as the ratio of the maximum cross-sectional area to the equivalent cross-sectional area of the bubble. Therefore, it can be predicted that the empirical correlation for bubble deformation can be described by a function of the relative velocity and sliding time. However, at this experiment, the relation of bubble deformation with relative velocity was not identified clearly, so the sliding time is adopted as parameter determining the degree of deformation. The function is defined as:

$$C_{deform} = \frac{1}{(1-0.0018t_{sl})} \quad (5-6)$$

where t_{sl} : sliding time.

5.1.3 Radius of curvature of the bubble at the heater surface

When the contact pressure force is calculated, the radius of curvature of the bubble at the heater surface, r_r , is required to estimate internal pressure of bubble.

In previous studies, the radius was defined as a constant ratio for the equivalent radius of bubble, and the ratio was decided depending on experimental observation. Thus, the function for the radius of curvature at the surface is described with the equivalent radius of bubble.

Unlike other geometries, however, the sliding bubble on horizontal tube is deformed significantly, changing the ratio for the equivalent radius. So the ratio is represented as function of bubble deformation as follows.

$$r_r = (2.1 - 1.06C_{deform})r_b \quad (5-7)$$

5.1.4 Contact angle

As contact angle between sliding bubble and heating wall is difficult to measure in experiment, it is mostly assumed as constant value. Nevertheless, in case of horizontal tube, the prediction of sliding bubble behavior depends on surface tension force, which is calculated by the contact angle. Thus, in this study, the contact angle, θ_c , is calculated by relation between the contact diameter and equivalent radius instead of assuming as constant, as shown in Fig. 5.2.

$$\theta_c = \frac{\pi}{2} - \cos^{-1} \left(\frac{d_w / 2}{r_r} \right) \quad (5-8)$$

In fact, there is a difference between advancing and receding contact angles, since the sliding bubble is inclined by drag force. The average difference was about 5 degrees in this experiment, and the contact angles are defined as below equations.

$$\alpha = \theta_c + 2.5 \text{ deg}, \beta = \theta_c - 2.5 \text{ deg} \quad (5-9)$$

5.1.5 Velocity gradient correction factor

As described in section 4.3, the local velocity gradient of liquid can be estimated by radial force balance analysis instead of experimental measurement, and it is expressed by the linear gradient multiplied by the correction factor. The correction factors are shown to be inversely proportional to the local liquid velocity, so it can be modeled by fitting the transient like as below equation.

$$f_c = -2.56V_{bulk}f^{1/2} + 0.75 \quad (5-10)$$

5.1.6 Limitation in the closure

In addition to the parameters modeled above, bubble volume and frequency are required to analyze the bubble behavior, so they were measured in this experiment. Unfortunately, however, they were not modeled in this study due to the following reasons.

As a result of experimental observation, the bubble frequency increases with increasing the heat flux and flow rate. However, it was difficult to be modeled, since the tendency of bubble frequency is somewhat irregular and intermittence.

Fig. 3.16 confirms that the bubble volume is closely related to the contact area of bubble and heating surface. The contact area decides the variation in the bubble volume, and the variation depends on the experimental conditions. Thus, the empirical correlation for bubble volume is described as function of the contact area multiplied by a coefficient determined by the given experimental conditions.

$$\frac{dV}{dt} = C_{grow}(V_{bulk} q/f^{1/2})A_{cont} \quad (5-11)$$

The experimental conditions determining the coefficient are local liquid

velocity, heat flux and bubble frequency, and the tendency was most clearly identified by $V_{bulk} q / f^{1/2}$ as shown in Fig. 5.3. When the local liquid velocity is faster, the bubble velocity is also faster. It means that the sliding length per unit time is extended, so the sliding bubbles receive heat from the wide heating area and grow rapidly due to promotion of evaporation. Furthermore, if the heat flux is higher and the bubble frequency is lower, the bubble volume changes rapidly, since there is a lot of heat conducted per bubble. Therefore, it appears that the tendency shown in Fig. 5.3 is reasonable.

However, despite the confirmation of this trend, the reason for the failure of the modelling is that the sensitivity of the force balance analysis to the bubble volume is too high. In the force balance analysis, the contact diameter is decided with considering the equivalent radius of the bubble, such as Equation (4-19). Thus, if the bubble volume is overestimated, the contact area becomes overestimated and the subsequent volume is calculated as larger value than actual bubble volume, and which makes the prediction of bubble volume completely different from reality. The other reason is that the rotation and deformation of sliding bubble are not considered in this analysis, so it is very difficult to deduce the contact area as practical. The bubble volume is hardly estimated correctly, since it is calculated by the contact diameter.

The limitation of the closure is expected to be overcome by finding applicable existing model for bubble volume or simplifying the transient of bubble volume.

5.2 Prediction result

Figs. 5.4 and 5.5 present the overlapped experimental images with the bubble trajectory, tracked using the force balance model with empirical correlations. The input data, required for the force balance model, are the heat flux, bulk liquid velocity, bubble frequency, volume and initial condition of bubble behavior, which consists of the bubble velocity, bubble location, contact diameter. As shown in overlapped images, the bubble trajectory can be predicted in a reasonable accuracy, regardless of the location of the nucleation site. The proximity to the heating wall after the lift-off is predicted similarly to experimental observation as well as the location and diameter at lift-off.

As a result of the prediction of the lift-off using the force balance model with empirical correlations, the prediction error of the sliding length is lower than $\pm 10\%$ and that of the lift-off diameter is lower than $\pm 4\%$ as represented in Fig. 5.6. The reason why the prediction error of the lift-off diameter is lower than that of the lift-off location is that the change of bubble volume is not significant near the lift-off.

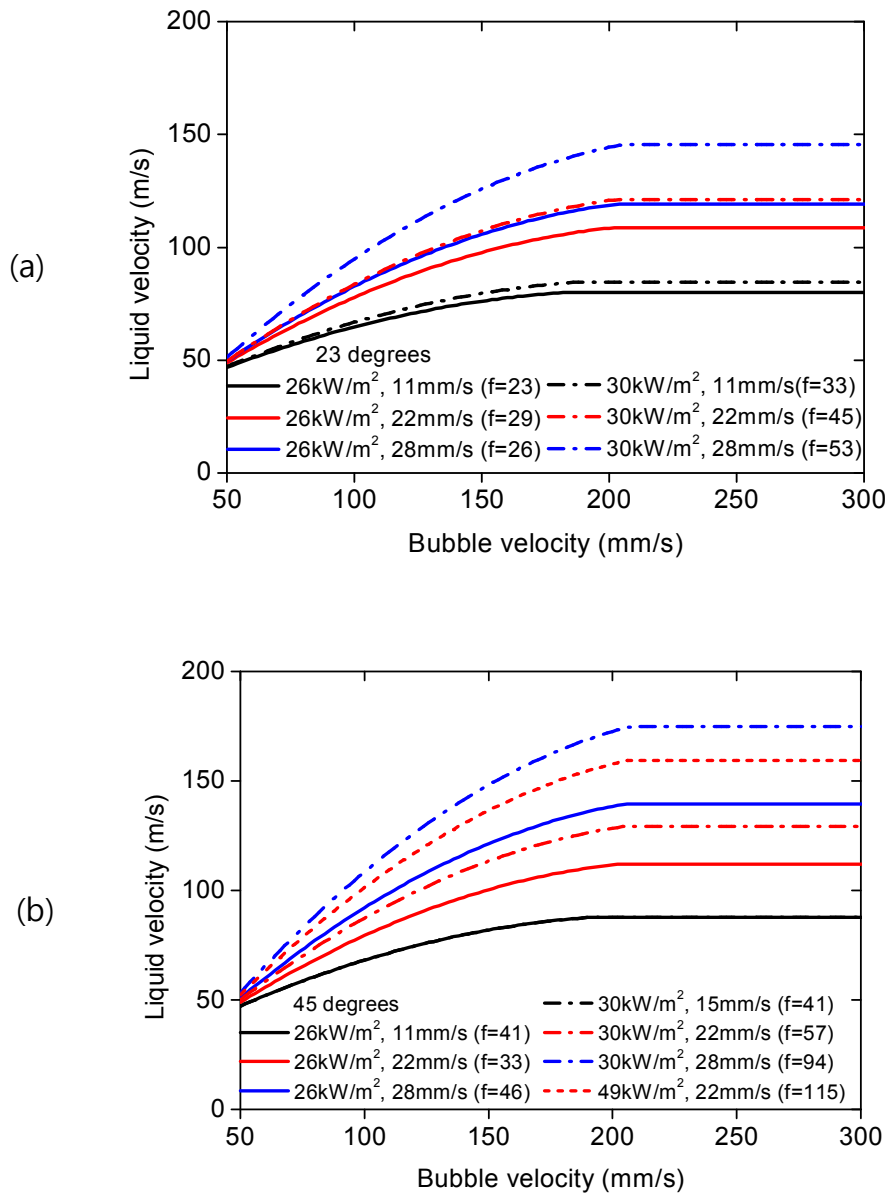


Figure 5.1 Empirical correlation of local liquid velocity: (a) 23° nucleation location, (b) 45° nucleation location.

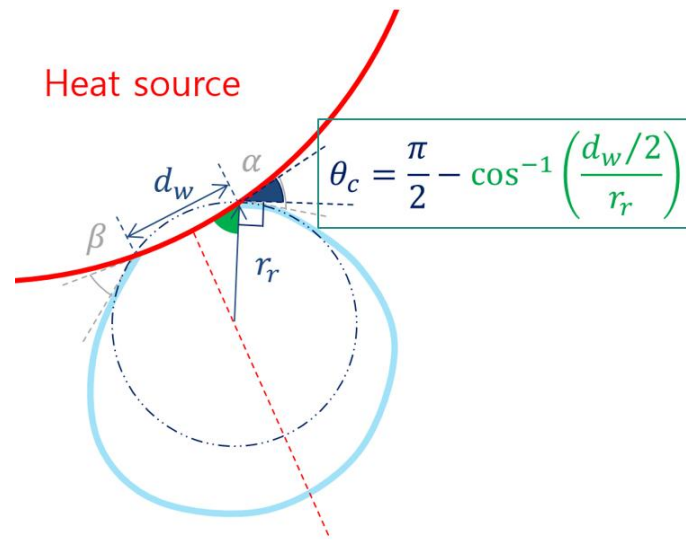


Figure 5.2 Schematic diagram about calculation of contact angle.

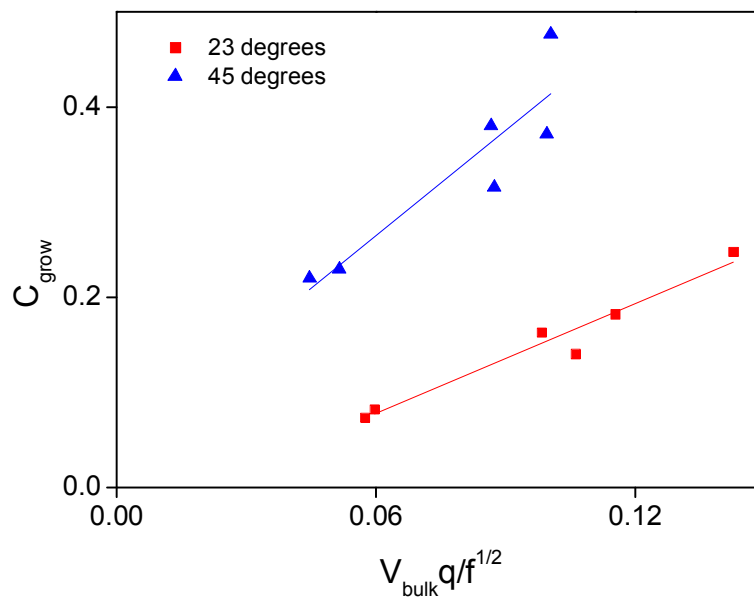
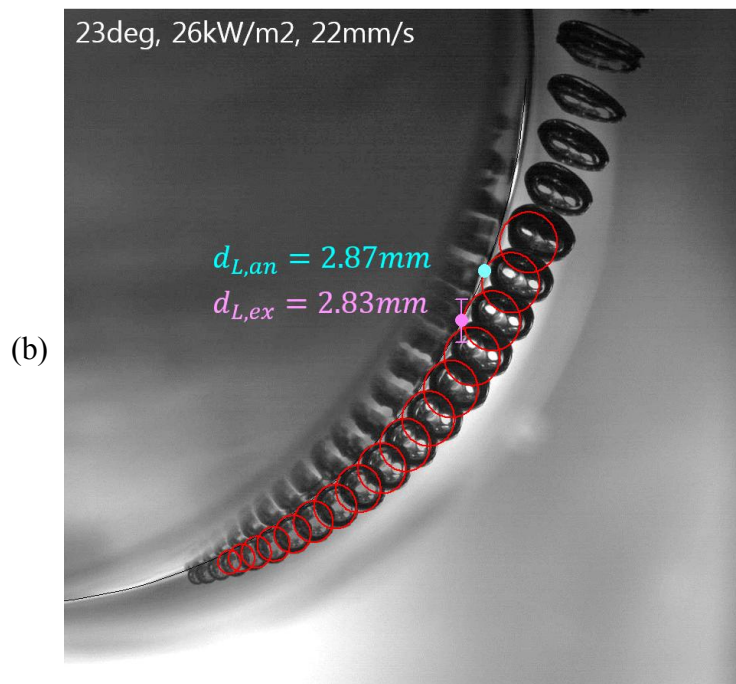
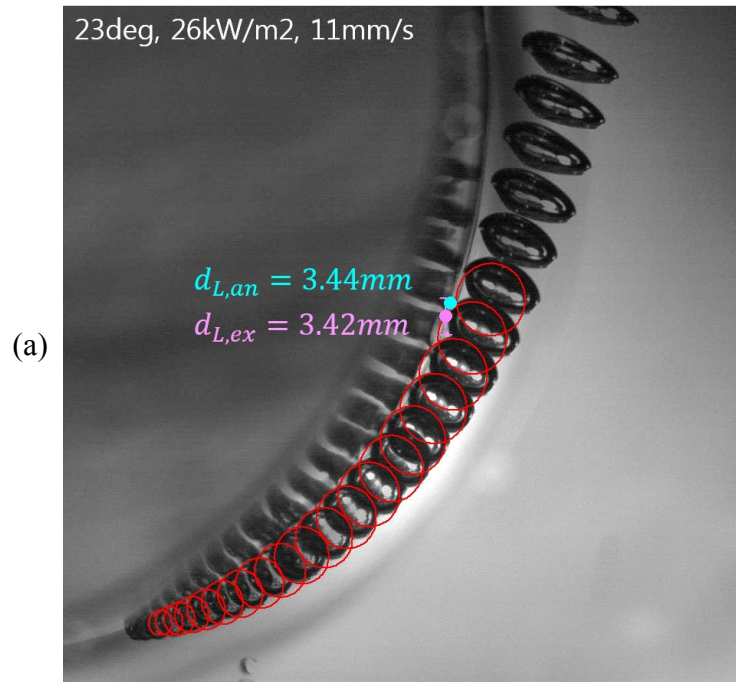
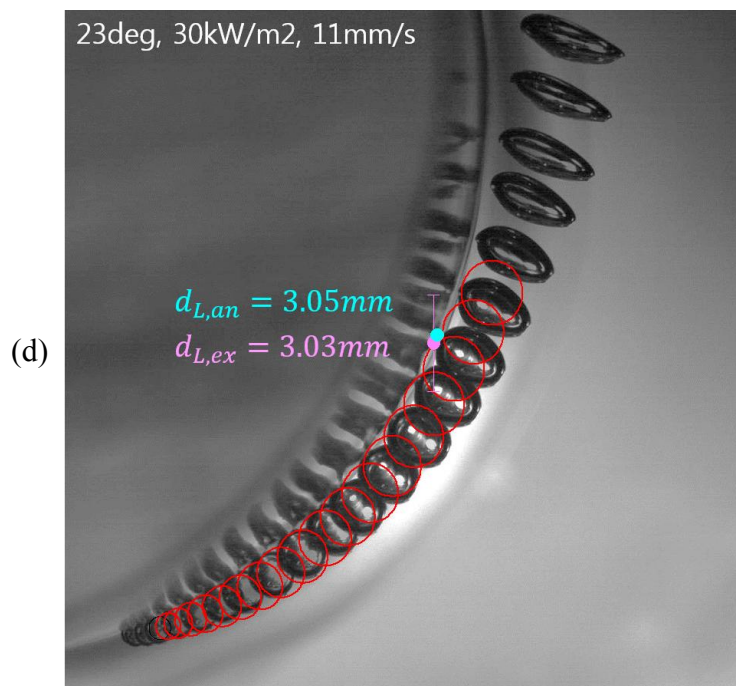
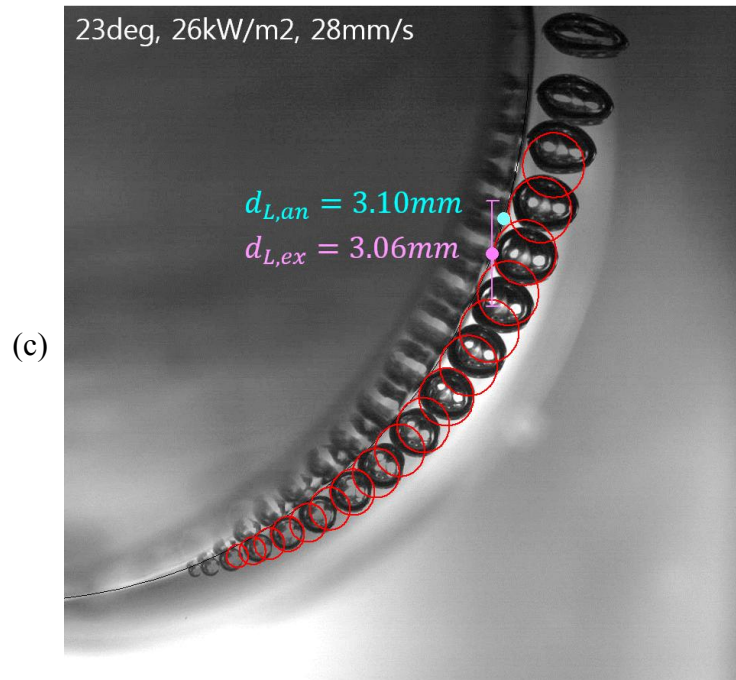


Figure 5.3 Coefficient in empirical correlation of bubble volume.





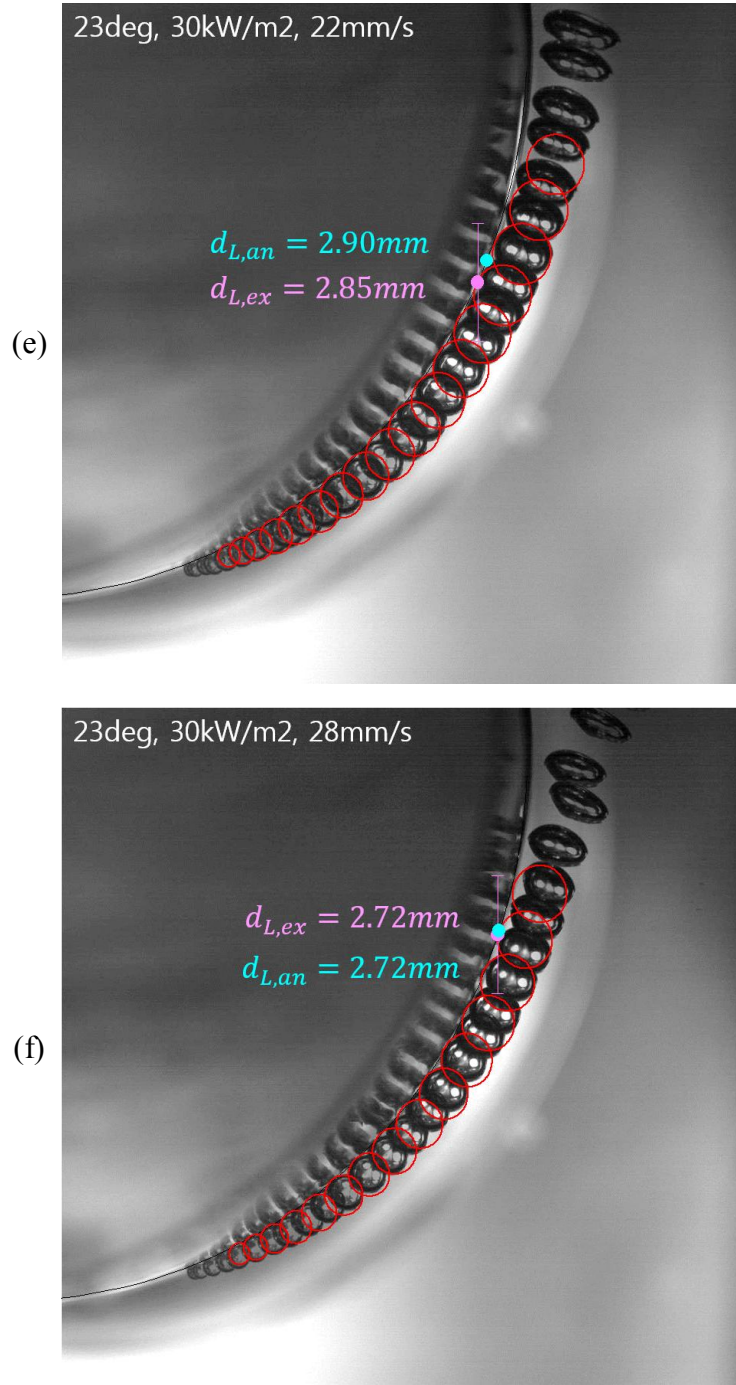
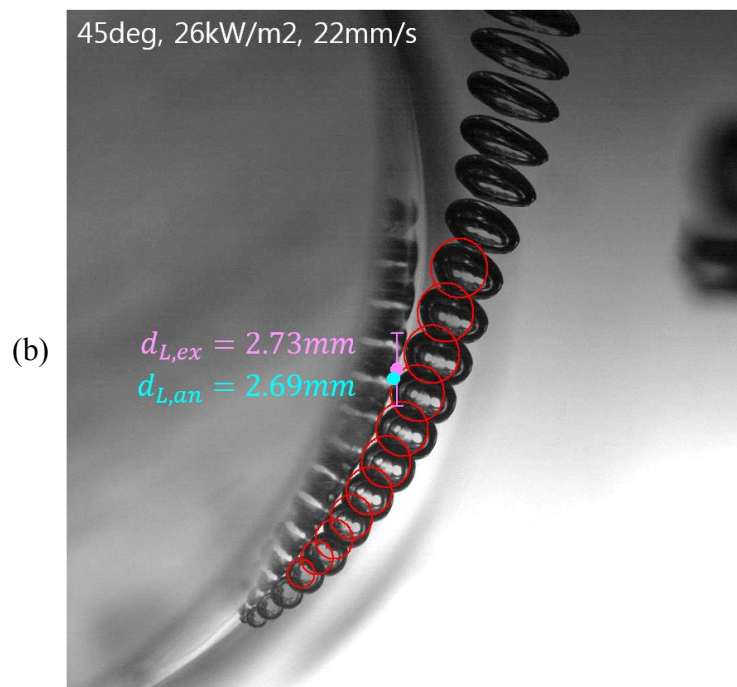
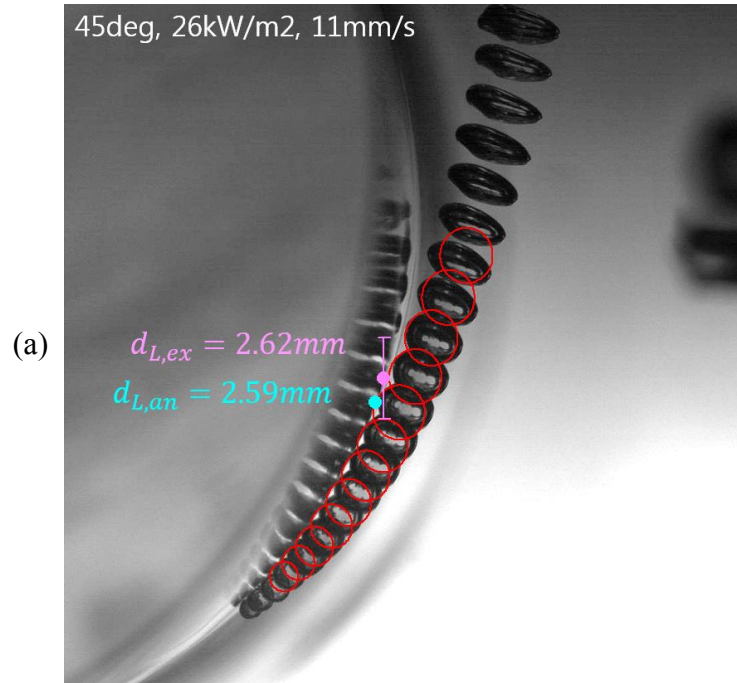
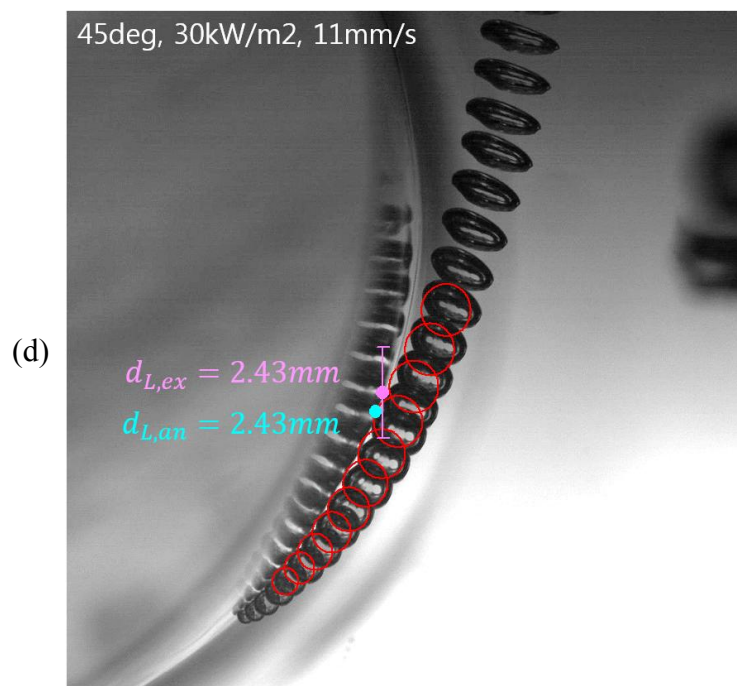
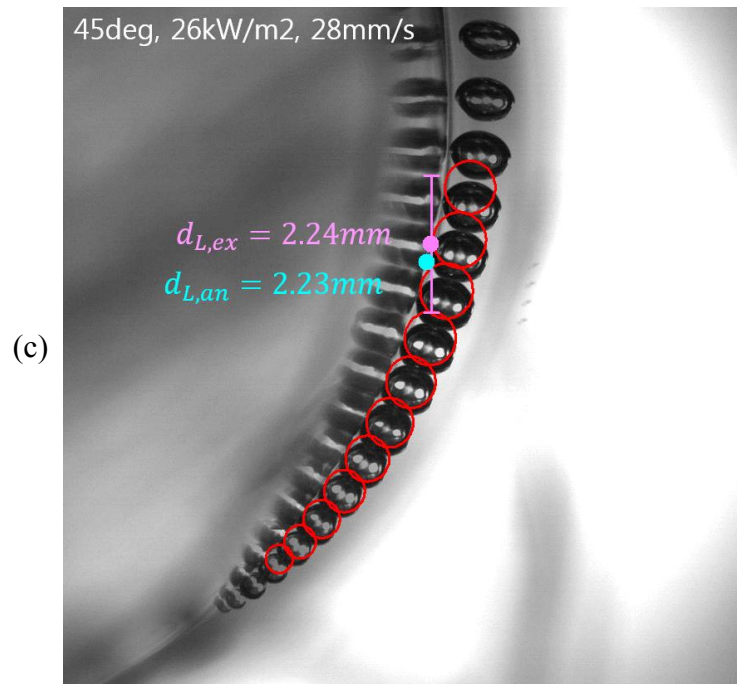
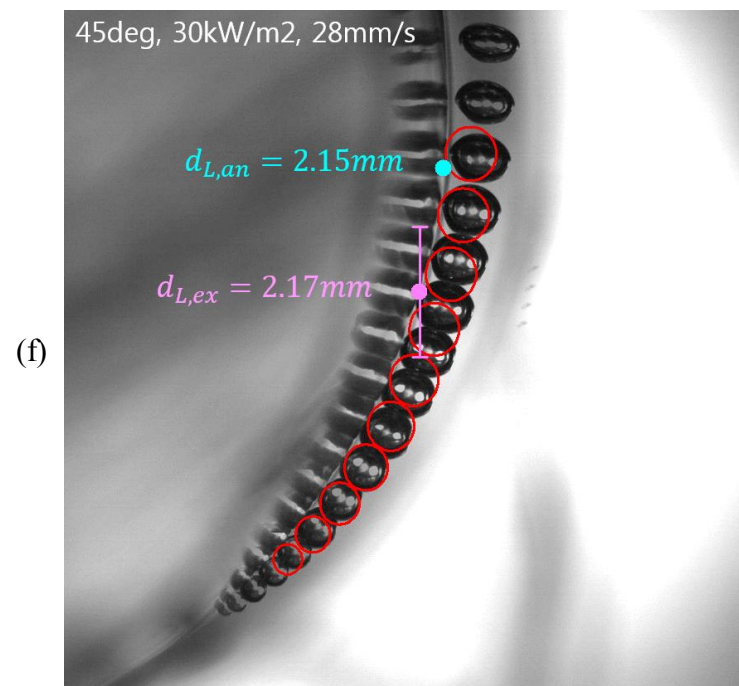
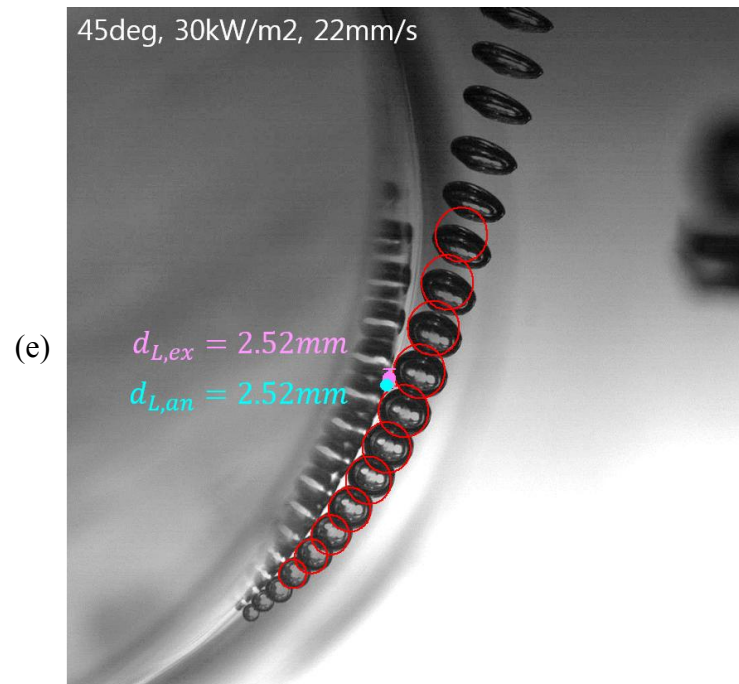


Figure 5.4 Bubble trajectory tracked by the force balance model with empirical correlations of 23° nucleation location: (a) 26kW/m², 11mm/s, (b) 26kW/m², 22mm/s, (c) 26kW/m², 28mm/s, (d) 30kW/m², 11mm/s, (e) 30kW/m², 22mm/s, (f) 30kW/m², 28mm/s.







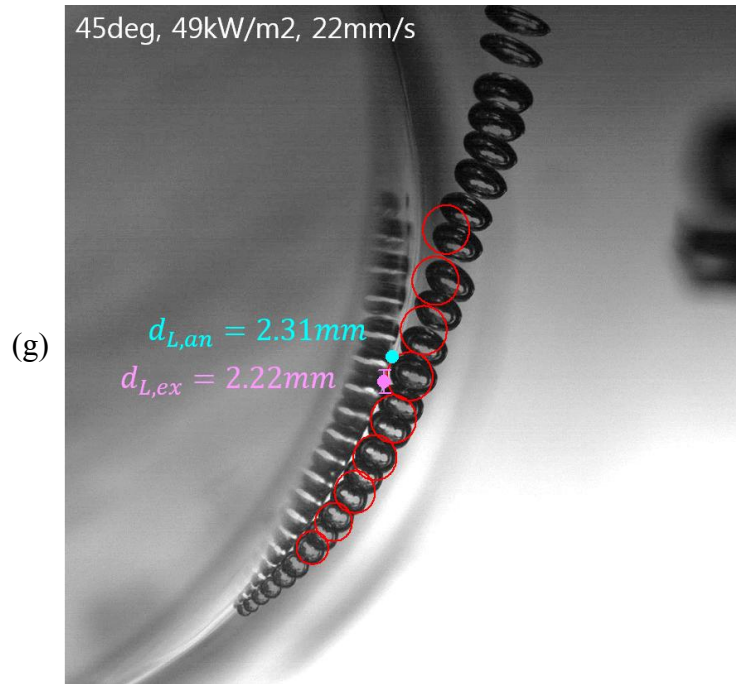


Figure 5.5 Bubble trajectory tracked by the force balance model with empirical correlations of 45° nucleation location: (a) 26kW/m², 11mm/s, (b) 26kW/m², 22mm/s, (c) 26kW/m², 28mm/s, (d) 30kW/m², 11mm/s, (e) 30kW/m², 22mm/s, (f) 30kW/m², 28mm/s, (g) 49kW/m², 22mm/s.

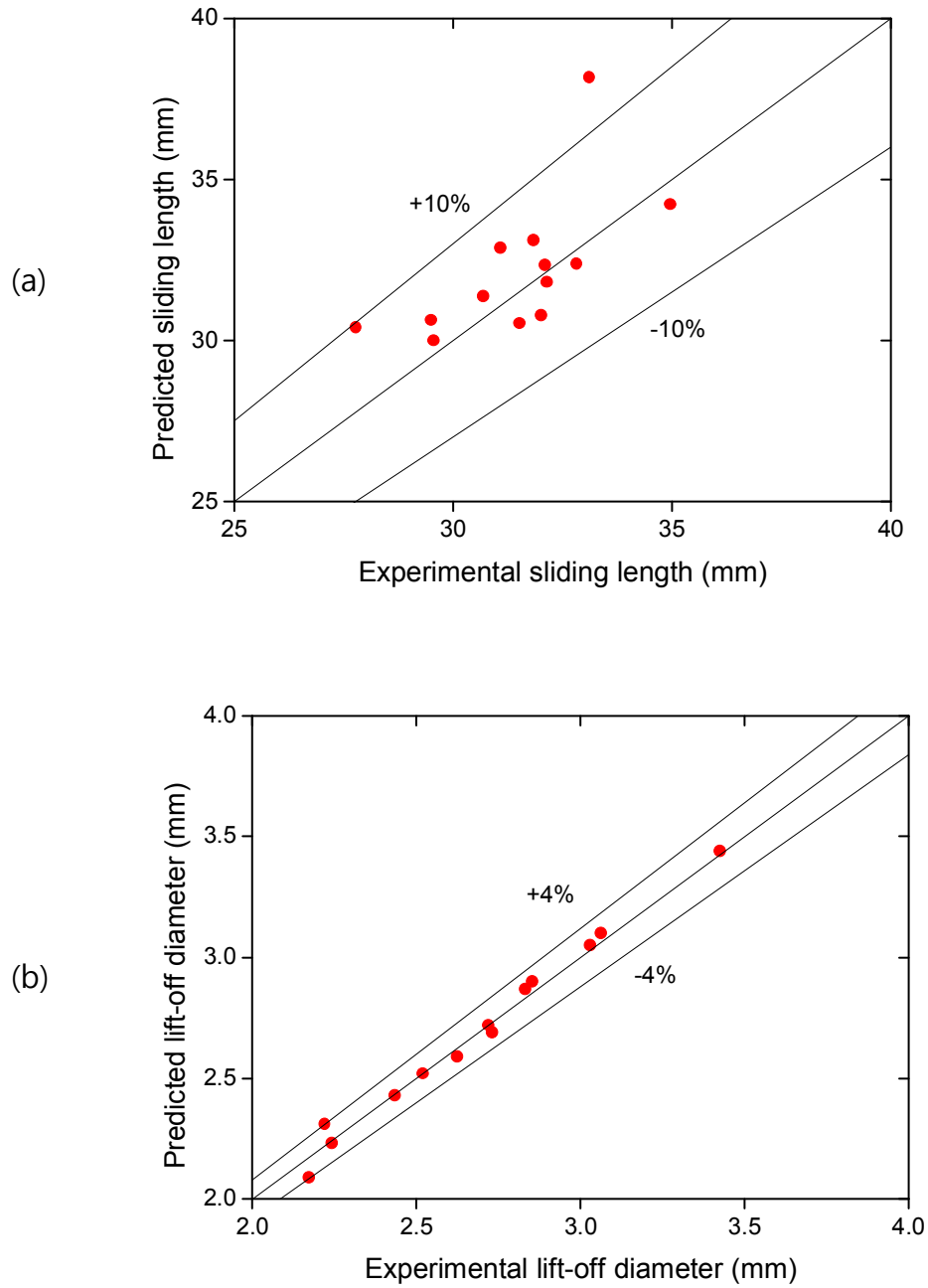


Figure 5.6 Prediction result of the improved force balance model with empirical correlations: (a) sliding length, (b) lift-off diameter.

Chapter 6.

Conclusion

6.1 Summary

In this study, the sliding bubble behavior on horizontal tube, required to improve the heat transfer model for horizontal tube, was measured by the measurement and visualization techniques, established for the sliding bubble on a curved surface. Then, the forces acting on the sliding bubble were analyzed in cylindrical coordinate to predict the bubble behavior. The achievements of this study can be summarized as follows:

1. Establishment of measurement and visualization techniques for sliding bubble
 - The narrow strip flexible heater was devised for visualization of sliding bubble behavior.
 - Various bubble parameters were measured by automatic image processing.
 - The stereoscopic bubble reconstruction technique has advantages for deformed bubble comparing with the monoscopic method.

2. Force balance analysis to understand sliding bubble behavior
 - Force balance model was improved for a sliding bubble on a horizontal tube by considering direction of forces and additional forces.
 - The dominant forces determining bubble behavior were identified.
3. Closure of force balance model
 - Most of the required bubble parameters were modeled on the measured parameters in this experiment.
 - The bubble trajectory and lift-off were predicted in a reasonable accuracy.

6.2 Recommendation

In present study, the film heater, fabricated on a polyimide substrate, was used. However, the surface characteristics of the polyimide are different with that of metal surface. It can cause phenomenological differences in boiling and bubble behaviors depending on the surface characteristics of the reference surface. Therefore, further investigation should be conducted using the metal surface heater.

In the process of closing the force balance model, the bubble volume and frequency were not modelled. The limitation of the closure is expected to be overcome by finding applicable existing model for bubble volume or simplifying the transient of bubble volume. In addition, the other parameters need to be simplified to apply in various experimental conditions.

Reference

- Basu, N., Warriar, G. R., Dhir, V. K., 2005. Wall heat flux partitioning during subcooled flow boiling: Part 1-Model Development. *Journal of heat Transfer*. 127(2), 131–140.
- Bian, Y., Dong, F., Zhang, W., Wang, H., Tan, C., & Zhang, Z., 2013. 3D reconstruction of single rising bubble in water using digital image processing and characteristic matrix. *Particuology*. 11(2), 170–183.
- Cho, S. H., Kim, S. H., Lee, J. G., & Lee, N. E., 2005. Micro-scale metallization of high aspect-ratio Cu and Au lines on flexible polyimide substrate by electroplating using SU-8 photoresist mask. *Microelectronic Engineering*. 77(2), 116-124.
- Chu, I. C., Lee, S. J., Youn, Y. J., Park, J. K., Choi, H. S., Euh, D. J., & Song, C. H., 2016. Experimental evaluation of local bubble parameters of subcooled boiling flow in a pressurized vertical annulus channel. *Nuclear Engineering and Design*.
- Cornwell, K., Schüller, R. B., 1982. A study of boiling outside a tube bundle using high speed photography. *International Journal of Heat and Mass Transfer*. 25(5), 683–690.
- Duan, X., Phillips, B., McKrell, T., & Buongiorno, J., 2013. Synchronized high-speed video, infrared thermometry, and particle image velocimetry data for validation of interface-tracking simulations of nucleate boiling phenomena. *Experimental Heat Transfer*. 26(2-3), 169-197.
- Fiorenza, G., Manzari, V., Pastore, C., Sgura, I., Torresi, M., Gargiulo, C., 2013. An innovative polyimide microchannels cooling system for the pixel sensor of the upgraded ALICE inner tracker. In: *Proceedings of the 5th IEEE International Workshop on Advances in Sensors and Interfaces (IWASI)*, Jun 13–14, 2013. Bari, Italy.
- Fujiwara, A., Danmoto, Y., Hishida, K., & Maeda, M., 2004. Bubble deformation and flow structure measured by double shadow images and PIV/LIF. *Experiments in Fluids*. 36(1), 157–165.
- Gotoh, K., Nakata, Y., Tagawa, M., & Tagawa, M., 2003. Wettability of ultraviolet excimer-exposed PE, PI and PTFE films determined by the contact angle measurements. *Colloids*

- and Surfaces A: Physicochemical and Engineering Aspects. 224(1), 165-173.
- Hahne, E., Barthau, G., 2000. Evaporation waves in flashing processes. *International Journal of Multiphase Flow*. 26(4), 531–547.
- Jeon, S. S., Hong, S. J., Cho, H. K., Park, G. C., 2015. Prediction of nucleate boiling heat transfer on horizontal U-shaped heat exchanger submerged in a pool of water using MARS code. *Nuclear Engineering and Design*. 295, 317–337.
- Jung, S., Kim, H., 2016. Effects of surface orientation on nucleate boiling heat transfer in a pool of water under atmospheric pressure. *Nuclear Engineering and Design*. 305, 347-358.
- Kang, K. H., Kim, S., Bea, B. U., Cho, Y. j., Park, Y. S., Yun, B. J., 2012. Separate and integral effect tests for validation of cooling and operational performance of the APR+ Passive Auxiliary Feedwater System. *Nuclear Engineering and Technology*. 44(6), 597–610.
- Kang, M. G., 2005. Local pool boiling coefficients on the outside surface of a horizontal tube. *Journal of Heat Transfer*. 127(8), 949–953.
- Kim, S. J., Park, G. C., 2011. Interfacial heat transfer of condensing bubble in subcooled boiling flow at low pressure. *International Journal of Heat and Mass Transfer*. 54(13), 2962–2974.
- Klausner, J. F., Mei, R., Bernhard, D. M., Zeng, L. Z., 1993. Vapor bubble departure in forced convection boiling. *International Journal of Heat and Mass Transfer*. 36(3), 651–662.
- Kurul, N., Podowski, M. Z., 1990. Multidimensional effects in forced convection subcooled boiling. *Proceedings of the Ninth International Heat Transfer Conference*. 2, 19–24.
- Luke, A., Gorenflo, D., 2000. Heat transfer and size distribution of active nucleation sites in boiling propane outside a tube. *International Journal of Thermal Sciences*. 39(9), 919–930.
- The Mathworks, Inc., 2014. *Matlab Image Processing Toolbox User's Guide (version 9.1)*, Natwick, MA.
- Maurus, R., Ilchenko, V., & Sattelmayer, T., 2004. Automated high-speed video analysis of the bubble dynamics in subcooled flow boiling. *International Journal of Heat and Fluid*

- Flow. 25(2), 149–158.
- Murai, Y., Matsumoto, Y., & Yamamoto, F., 2001. Three-dimensional measurement of void fraction in a bubble plume using statistic stereoscopic image processing. *Experiments in Fluids*. 30(1), 11–21.
- Okawa, T., Ishida, T., Kataoka, I., Mori, M., 2005. Bubble rise characteristics after the departure from a nucleation site in vertical upflow boiling of subcooled water. *Nuclear Engineering and Design*. 235(10), 1149–1161.
- Qiu, D., Dhir, V. K., 2002. Experimental study of flow pattern and heat transfer associated with a bubble sliding on downward facing inclined surfaces. *Experimental Thermal and Fluid Science*. 26(6), 605–616.
- Rousselet, Y. L., 2014. Interacting Effects of Inertia and Gravity on Bubble Dynamics.
- Ryu, S.U., Kim, S., Euh, D.J., 2014. Development of Lift-Off Diameter Model of Bubbles Generated on Horizontal Tube. In: ASME 2014 International Mechanical Engineering Congress and Exposition. American Society of Mechanical Engineers, p. V08BT10A055-V08BT10A055.
- Sateesh, G., Das, S. K., Balakrishnan, A. R., 2005. Analysis of pool boiling heat transfer: effect of bubbles sliding on the heating surface. *International Journal of Heat and Mass Transfer*. 48(8), 1543–1553.
- Situ, R., Hibiki, T., Ishii, M., Mori, M., 2005. Bubble lift-off size in forced convective subcooled boiling flow. *International Journal of Heat and Mass Transfer*. 48(25), 5536–5548.
- Situ, R., Ishii, M., Hibiki, T., Tu, J. Y., Yeoh, G. H., Mori, M., 2008. Bubble departure frequency in forced convective subcooled boiling flow. *International Journal of Heat and Mass Transfer*. 51(25), 6268–6282.
- Sugrue, R., Buongiorno, J., McKrell, T., 2014. An experimental study of bubble departure diameter in subcooled flow boiling including the effects of orientation angle, subcooling, mass flux, heat flux, and pressure. *Nuclear Engineering and Design*. 279, 182–188.
- Thorncroft, G. E., Klausner, J. F., Mei, R., 1998. An experimental investigation of bubble

- growth and detachment in vertical upflow and downflow boiling. *International Journal of Heat and Mass Transfer*. 41(23), 3857–3871.
- Thorncroft, G. E., & Klausner, J. F., 2001. Bubble forces and detachment models. *Multiphase Science and Technology*, 13(3&4).
- Van Helden, W. G. J., Van der Geld, C. W. M., & Boot, P. G. M., 1995. Forces on bubbles growing and detaching in flow along a vertical wall. *International journal of heat and mass transfer*, 38(11), 2075-2088.
- Yeoh, G. H., Tu, J. Y., 2004. Population balance modelling for bubbly flows with heat and mass transfer. *Chemical Engineering Science*. 59(15), 3125–3139.
- Yoo, J., Estrada-Perez, C. E., Hassan, Y. A., 2014. A proper observation and characterization of wall nucleation phenomena in a forced convective boiling system. *International Journal of Heat and Mass Transfer*. 76, 568–584.
- Yun, B. J., Splawski, A., Lo, S., Song, C. H., 2012. Prediction of a subcooled boiling flow with advanced two-phase flow models. *Nuclear Engineering and Design*. 253, 351–359.
- Zaruba, A., Lucas, D., Prasser, H. M., & Höhne, T., 2007. Bubble-wall interactions in a vertical gas–liquid flow: Bouncing, sliding and bubble deformations. *Chemical Engineering Science*. 62(6), 1591–1605.

국문 초록

수평관 외벽에서의 비등은 APR+의 피동잔열제거계통인 PAFS 를 포함하여 다양한 시스템에서 발생한다. 열분배 모델과 같은 기구학적 모델을 통해 비등 열전달을 예측하기 위해서는 비등 기포의 거동을 파악하는 것이 중요하고, 특히 수평관 하부와 같은 하부 경사면의 경우 활주 기포의 효과가 열전달률 예측의 정확도에 영향을 준다. 하지만 지금까지의 기포 거동에 대한 연구는 주로 수평면 또는 수직관에 대하여 이루어져 수평관 외벽의 활주 기포 거동에 대한 실험적, 이론적 연구가 부족한 상황이다. 따라서 본 연구는 수평관 열전달 모델 개선에 필요한 활주 기포 거동 변수를 실험적으로 관측하고, 개선된 힘평형 모델을 통해 활주 기포 거동을 정확히 분석하여 예측 가능 모델의 기반을 마련하는 것을 목표로 하였다.

먼저 수평관 외벽 활주 기포 거동을 관측하기 위하여 실험 장치를 구성하고, 2 개의 고속카메라를 이용한 양방향 관측 기법을 수립하였다. 실험은 대기압 포화 비등을 대상으로 하였으며 유속은 11.2-27.6mm/s, 열속은 26-66 kW/m², 핵비등 생성 지점의 위치는 0-180°로 다양한 실험 조건에서 진행되었다. 비등이 일어나는 수평관 히터는 3mm 의 얇은 띠모양 가열부를 포함한 FPCB 히터를 50mm 지름의 폴리카보네이트에 부착하여 제작하였다. 이렇게 제작된 히터는 활주 기포 가시화를 용이하게 하였다. 또한 가열부 위에 인위적으로 핵비등 생성지점을 생성하였는데, 이를 통해 단일 기포 생성 지점을 통제하고 폴리에이미드 기반 히터의 표면 조건 차이를 개선할 수 있었다.

동기화된 2 개의 고속카메라는 각각 수평관 히터의 축 방향과 측면 방향에서 기포 거동을 관측하였는데, 이 관측 이미지로부터 기포의 이탈 및 부상, 부피, 속도, 주기 등 다양한 활주 기포 거동 변수를 도출하였다. 본

연구에서 활주 기포 거동 관측을 위해 수립하고 활용된 관측 기법은 크게 두 가지로 상분리 기법과 3 차원 재구성 기법이다. 특히, 기포 부피 측정에 있어서 본 연구에서 제시한 양방향 3 차원 재구성 기법이 기존의 단일 방향 측정 기법에 비하여 그 정확도가 높다는 것이 명확히 검증되었다.

이 실험적 관측 결과를 기반으로 수평관 위 활주 기포에 작용하는 힘 평형 분석을 진행하였다. 이를 위하여 기존의 수평면 위 활주 기포를 대상으로 한 힘 평형 모델을 수평관 위 활주 기포에 적용 가능하도록 추가적인 힘을 도입하고 원통 좌표계로 표현하였다. 이때 원주 방향 힘 평형 분석은 실험적으로 관측하지 못한 액체의 국부 속력을 추정하는데 활용하였고, 반지름 방향 힘 평형 분석은 기포의 부상 지점을 예측하고 액체의 국부 속도 기울기를 추정하는데 활용하였다. 분석 결과, 기포 거동을 결정하는 지배적인 힘들을 파악할 수 있었다. 기포가 활주할 때는 표면장력, 접촉 압력에 의한 힘, 부력과 부가 질량에 의한 힘이 주요하게 작용하며, 부상 시에는 양력, 부력 및 부가 질량에 의한 힘이 주요한 힘으로 분석된다. 마지막으로, 실험 관측 및 분석 결과를 바탕으로 기포 거동 변수의 경향성을 파악하고 이를 함수로 표현하였다. 이는 단순화 및 개선을 거쳐 기포 거동 예측 모델 개발의 기반이 될 수 있을 것이라 기대된다.

주요어

비등 열전달, 수평관, 활주 기포 거동, 양방향 관측 기법, 이미지 처리 기법, 힘 평형 분석.

학번: 2015-22940